HHS Public Access

Author manuscript

ACS Chem Biol. Author manuscript; available in PMC 2026 January 13.

Published in final edited form as:

ACS Chem Biol. 2025 November 21; 20(11): 2808–2826. doi:10.1021/acschembio.5c00753.

Exploring Metalloproteome Remodeling in Calprotectin-Stressed *Acinetobacter baumannii* Using Chemoproteomics

Maximillian K. Osterberg[¶],
Department of Chemistry, Indiana University, Bloomington, Indiana 47405-7102, United States

Daniel W. Bak[¶],
Department of Chemistry, Boston College, Chestnut Hill, Massachusetts 02467-3860, United States

Claudia Andreini,
Magnetic Resonance Centre (CERM), University of Florence, Florence, Sesto Fiorentino 50019, Italy

Minyong Kim,
Department of Chemistry, Indiana University, Bloomington, Indiana 47405-7102, United States

Jeanette M. Critchlow,
Department of Pathology, Microbiology, and Immunology, and Vanderbilt Institute for Infection, Immunology, and Inflammation, Vanderbilt University Medical Center, Nashville, Tennessee 37232, United States

Jonathan C. Trinidad,
Laboratory for Biological Mass Spectrometry, Department of Chemistry, Indiana University, Bloomington, Indiana 47405-7102, United States

Peter V. Cornish,
Department of Biochemistry, University of Missouri, Columbia, Missouri 65211, United States

Tae Akizuki,
Departments of Biochemistry and of Chemistry, and Center for Structural Biology, Vanderbilt University, Nashville, Tennessee 37240, United States

Walter J. Chazin,
Departments of Biochemistry and of Chemistry, and Center for Structural Biology, Vanderbilt University, Nashville, Tennessee 37240, United States

Corresponding Authors: **Eranthie Weerapana** – Department of Chemistry, Boston College, Chestnut Hill, Massachusetts 02467-3860, United States; eranthie@bc.edu, **David P. Giedroc** – Department of Chemistry, Indiana University, Bloomington, Indiana 47405-7102, United States; giedroc@iu.edu.
[¶]M.K.O. and D.W.B. contributed equally to this work.

Author Contributions

M. K. O., with some assistance from M. K. early in the project, carried out the analysis and biochemical validation of the chemoproteomics data acquired by D. W. B. under the supervision of E. W. on biological samples provided by M. K. O. M. K. O. performed the all label-free proteomics experiments in collaboration with J. C. T. and P. V. C. J. M. C. and E. P. S. provided the Δ*zigA* strain used in this sudy and T. A. and W. J. C. provided the calprotectin used in this study. M. K. O. and D. P. G. wrote the manuscript with editorial input from all other authors.

The authors declare no competing financial interest.

Complete contact information is available at: https://pubs.acs.org/10.1021/acschembio.5c00753

Eric P. Skaar,
Department of Pathology, Microbiology, and Immunology, and Vanderbilt Institute for Infection, Immunology, and Inflammation, Vanderbilt University Medical Center, Nashville, Tennessee 37232, United States

Eranthie Weerapana,
Department of Chemistry, Boston College, Chestnut Hill, Massachusetts 02467-3860, United States

David P. Giedroc
Department of Chemistry, Indiana University, Bloomington, Indiana 47405-7102, United States

Abstract

The growth of bacterial pathogens is limited by nutritional immunity, where the infected host deploys transition metal scavenging proteins including calprotectin (CP) to starve the bacterium of essential transition metals. Prior work reveals that CP induces a significant Zn- and Fe-starvation response in the Gram-negative opportunistic pathogen *Acinetobacter baumannii* in liquid culture. Here, we employ a quantitative chemoproteomics platform to pinpoint changes in abundance-corrected cysteine reactivity— and by extension cellular metal occupancy in metalloenzymes—that occur when *A. baumannii* is challenged with physiological CP in liquid culture relative to an untreated WT control. Changes in protein abundance with CP stress reveal a pronounced Zn-limitation and Fe-starvation response and reciprocal regulation of three enzymes of central carbon metabolism, including aconitase. A majority of the 2645 quantifiable Cys-containing peptides that show an increase in abundance-corrected Cys reactivity (150) are derived from known Zn-, Fe-, and Fe–S-cluster proteins, revealing a significant decrease in metal occupancy (undermetalation) across the proteome. Myriad cell processes are impacted by undermetalation, including enzymes that function in the TCA cycle and respiration, GTP metabolism, ribosome remodeling, tRNA charging, and proteostasis. In an effort to identify an undemetalated client enzyme for the candidate GTPase-powered metallochaperone ZigA, we performed this chemoproteomics experiment in a CP-stressed Δ*zigA* strain relative the CP-stressed wild-type strain. These findings reveal that the loss of ZigA is effectively silent in this assay. We conclude that CP induces a widespread, negative impact on the metalation status of the metalloproteome that results in a significant nutrient limitation response.

Graphical Abstract

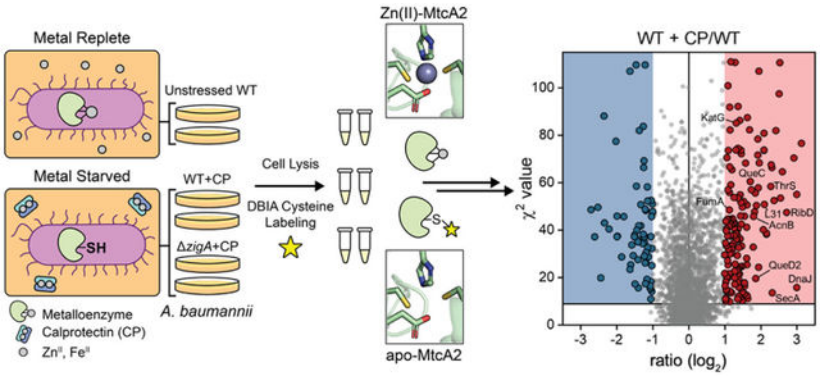

INTRODUCTION

The emergence of widespread antimicrobial resistance (AMR) to conventional and last-resort antibiotic therapies continues to complicate efforts to combat bacterial infectious disease in humans.[1,2] One attractive approach to meet this challenge is to identify metabolic pathways in bacterial pathogens that become critical only during the course of an infection, in an adaptive often bacteriostatic response to host efforts to minimize dissemination from the initial site of colonization. This might ultimately lead to optimal deployment of myriad antimicrobial weapons by the host that are used to clear the invading pathogen. Targeting specific aspects of bacterial metallostasis,[3] a term encompassing all processes that maintain the integrity of the metalloproteome upon challenge by metal limitation or metal toxicity,[4–6] might be one such strategy to aid development of new antibacterial therapeutic strategies.[3,7]

An important antimicrobial response of the innate immune system toward extracellular pathogens is the deployment of transition metal-sequestering proteins that limit the availability of transition metals to the bacterium at sites of infection. This induces a metal starvation response in a process known as nutritional immunity.[4,8,9] Originally discussed in the context of host nutrient Fe(III)-limitation mediated by lactoferrin, which binds Fe(III), and lipocalin-2, which binds Fe(III)-siderophore complexes, nutritional immunity against invading pathogens is now known to extend to other first-row *d*-block metals including Mn(II) and Zn(II) as well as Fe(II).[10–14] A number of S100 subfamily EF-hand Ca(II)-binding proteins play roles in host nutritional immunity by binding Zn(II) and Cu(II) at transition-metal binding sites distinct from their Ca(II) binding sites.[15] The S100A8/S100A9 heterotetramer, calprotectin (CP),[15,16] is a unique member of this subfamily, well characterized for its participation in the “tug-of-war” between pathogen and host for nutrient metals.[17] CP harbors two pairs of high-affinity transition-metal coordination sites: One is a His_3-Asp site that is common to other S100 proteins,[15,18,19] while the other is an octahedral hexahistidine (His_6) site found only in CP, which chelates Zn(II),[20] Cu(II),[21] Mn(II),[22] Ni(II)[23] and Fe(II).[24] While the transition metal-sequestering role of CP is paramount to its function, evidence has emerged to suggest that CP induces a cell wall stress response that is independent of its role in metal sequestration.[25,26] These findings largely derive from bacterial growth experiments in liquid culture in the presence of wild-type and mutant CP derivatives.

It is well-established that bacteria cultured in the presence of CP are starved for transition metals in a way that appears strongly dependent on the culture conditions and the organism itself.[15] We have long been interested in how the Gram-negative opportunistic and nosocomial pathogen, *Acinetobacter baumannii*, responds to CP-mediated stress.[27–33] Early bacterial cell culture and metal add-back experiments revealed that CP induces Zn(II)-starvation in *A. baumannii* given the strong transcriptional up-regulation of the Zur (zinc-uptake repressor) regulon.[28,34] A major Zur-regulated gene encodes a cluster of orthologous groups (COG) 0523 superfamily candidate metallochaperone, Zur-induced GTPase A (ZigA). ZigA appears to impact bioavailable Zn in *A. baumannii* cells in a way that is connected to histidine catabolism and is required for disseminated infections in mice.[27] While the biochemical properties of ZigA as a Zn-activated G-protein “switch” are

gaining clarity,[35] its function in cells and positive identification of a specific metalloenzyme client(s) for *Ab*ZigA remain unknown.

More recent global transcriptomics and proteomics experiments revealed that CP drives a Fe-starvation response superimposed on the Zn-limitation response.[27,33] These studies also established that one of the metabolic responses to low Fe availability is the prioritization of flavin biosynthesis, and evidence was presented for a "work-around" strategy allowing cells to accumulate high levels of flavin required for electron transfer that might be compromised as a result of a decrease in Fe-containing ferredoxins.[33] In addition, these studies hinted at a failure or prioritization of queuosine-tRNA biosynthesis, given the increased cellular abundance of the 6-carboxy-5,6,7,8-tetrahydropterin (6-CPH_4) synthase (QueD2) which catalyzes the rate-determining step in this pathway; it was subsequently shown that CP treatment reduces flux through the queuosine-tRNA biosynthesis pathway.[36] Queuosine (Q) is a hypermodified 7-deazaguanosine derivative[37,38] found in the anticodon loop of four tRNAs (tRNA) and is upregulated under nutrient-limitation and metal-limitation stress responses in other bacteria and organisms.[39,40] The Q substitution is known to impact tRNA structure and function in a way that can affect the rate and/or fidelity of translation and ultimately the composition of the proteome.[41]

The set-point model for transition metal homeostasis predicts that CP impacts bacterial metabolism by impairing the ability of the cellular milieu to supply metalloproteins with their cognate metal or metal cofactor.[42,43] This model predicts widespread undermetalation of some or all the metalloproteome,[3,42] as has been demonstrated for selected metalloenzymes in a small number of organisms.[23,44,45] The extent to which the metalloproteome is globally impacted in this way is currently unknown. Here, we employ a quantitative chemoproteomics platform to elucidate changes in abundance-corrected cysteine (Cys) reactivity that result when *A. baumannii* is exposed to CP in liquid culture relative to an untreated control. Metal–liganding cysteines in a metalloprotein become more reactive toward an electrophile upon metal dissociation, since metal-coordination attenuates the nucleophilicity of that cysteine.[46–49] Thiolate ligands are ubiquitous components of Fe–S cluster-containing proteins and a subset of Zn-metalloprotein sites, and as a result changes in the reactivity of these cysteines can act as a proxy for cellular metallocofactor occupancy.[50] Strong support for this hypothesis derives from pioneering studies of Fe–S protein biogenesis in *Escherichia coli*,[51–53] and examination of the effects of the thiophilic metal-chelating prodrug holomycin in *E. coli*.[54]

We reasoned that this chemoproteomic workflow could be used to globally probe metallocofactor occupancy in CP-treated *A. baumannii*, leveraging the finding that CP induces a Zn- and Fe-limitation regulatory response in this organism.[33,36] Using an isobaric mass spectrometry-based tagging strategy to quantify protein abundance, we show that pairs of enzymes involved in central carbon metabolism show reciprocal changes in protein abundance. These include two pairs of TCA cycle enzymes, aconitase[55] and fumarase,[54] a Zn- vs Fe-type alcohol dehydrogenase, and the ribosomal proteins L31 and the low-zinc paralog L31B,[56,57] these findings are consistent with a classical metal-sparing response.[58,59] In total, 29 Zn and Fe–S cluster proteins were found to exhibit a statistically significant ≥ 2-fold increase in the reactivity of metal-coordinating cysteines, including

22 Zn-metalloenzymes and 7 Fe–S cluster proteins. Undermetalation of Fe–S proteins negatively impacts their cell abundance, potentially consistent with increased turnover and more global Fe sparing, in contrast to the vast majority of undermetalated zinc enzymes, which display minimal changes in cell abundance. These undermetalated enzymes function in energy metabolism and respiration, GTP metabolism, ribosome remodeling and tRNA charging, RNA metabolism and proteostasis. In addition, ribosomes from CP-stressed cells exhibit classical hallmarks of ribosome hibernation and nutrient limitation.[60] These findings are broadly recapitulated in a strain lacking the candidate Zur-regulated metallochaperone, ZigA,[27,35,61] leaving unknown any potential metalloenzyme client for this GTPase.

RESULTS

Experimental Strategy.

In this work, we employed a 6-plex amine-reactive tandem mass-tag (TMT)-labeling approach coupled with desthiobiotin iodoacetamide (DBIA) Cys-labeling and streptavidin-agarose biotin enrichment for sequential quantification of protein abundance and abundance-corrected cysteine-reactivity changes in CP-stressed vs unstressed *A. baumannii* ATCC 17978-VU cells grown on a rich (Luria Broth), Ca(II)-supplemented growth medium with vigorous aeration (Figure 1). Biological duplicate bacterial cell lysates containing both soluble and membrane-associated proteins were obtained for untreated wild-type (WT), CP (300 μg/mL)-stressed WT and CP-stressed Δ*zigA* cells (six samples total) and subjected to DBIA labeling and protein isolation, digested with trypsin and subjected to 6-plex TMT labeling using the scheme indicated (Figure 1). The six samples were combined together and one part of the combined sample (≈25% of the total; in technical duplicate) was subjected directly to isobaric mass-spectrometry analysis to quantify relative protein abundance across each TMT channel. This experimental workflow thus provides a quantitative read-out of the relative changes in protein abundance in three pairwise comparisons (measured across four replicate channels per biological condition): 1) WT vs WT+CP; 2) WT vs Δ*zigA* + CP, and 3) WT + CP vs Δ*zigA* + CP in an approach analogous to label-free proteomics experiments published earlier.[33] This concentration of CP is sufficient to significantly sequester Zn, Fe(II), and Mn from the media (Figure S1A), yet induces only a significant ≈2-fold decrease in total cell-associated Zn as measured by inductively coupled plasma-mass spectrometry (ICP-MS), with little corresponding change in total cell-associated Fe despite these cells being significantly Fe-starved[33] (Figure S1B).

The remainder of the combined sample (75% of the total; in technical triplicate) was subjected to streptavidin enrichment and elution, with the relative abundance of individual eluted peptides again quantified by reporter-ion intensity. This provides relative quantitation of the abundance of Cys-containing peptides across the same three pairwise comparisons (measured across six replicate channels per biological condition). Normalizing these cysteine-reactivity changes against the changes in protein abundance, a net change in Cys reactivity is obtained as proxy for the relative change in fractional metal occupancy for a given metalloprotein.[49,52,54] Only those changes in net Cys reactivity greater than 2-fold ($\log_2 = \pm 1$) with a χ^2 cutoff of 9.0 were generally considered of primary significance here,

although in selected instances we discuss changes with slightly lower values ($\log_2 = \pm 0.64$; $\chi^2 \geq 9.0$).

We used MetalPredator,[62] the metalPDB database[63] and related tools with manual curation to estimate the number of Zn metalloproteins and Fe–S cluster proteins in the *A. baumannii* ATCC 17978-VU proteome to provide context for the findings reported here. We predict the presence of 225 zinc metalloproteins (comparable to 215 predicted previously[33]), of which 40% (87) contain at least one cysteine in the first coordination shell (Document S1). Of these 87 Zn proteins, 6 contain a single Cys, 11 contain two Cys, 22 contain three Cys, and 50 are tetrathiolate coordination sites that are known or anticipated to bind Zn, but if not previously characterized, could also potentially coordinate a 4Fe-4S cluster.[64] Likewise, we estimate the presence of 92 Fe–S-cluster proteins in *A. baumannii* ATCC 17978-VU (Document S1). We note that *A. baumannii*, like *Pseudomonas aeruginosa*, contains the minimal complement of ISC enzymes required to assemble both [2Fe-2S] and [4Fe-4S] proteins,[65] including the cysteine desulfurase IscS, the scaffolding protein IscU, the Fe–S cluster carriers IscA, ErpA, and NfuA,[66] as well as two copies of the regulatory protein IscR.[67] There is no "stress-responsive" SUF Fe–S cluster biogenesis system in *A. baumannii* like that found in *E. coli*.[53] In all, we were able to detect 147 (65%) known or predicted Zn enzymes and 59 (64%) known or predicted Fe–S cluster proteins in the proteome (Figure 2A). These percentages represent excellent coverage, since they are slightly higher than the fraction of the total *A. baumannii* proteome detected in these experiments (1966 proteins or 52%); we note however that there may be unidentified Zn and Fe–S cluster proteins that were not predicted by this analysis.

Changes in Protein Abundance in CP-Stressed *A. baumannii*.

A volcano plot illustrating the impact of CP stress on the WT *A. baumannii* proteome shows major perturbations of the proteome. Of the 1966 total proteins detected, 141 proteins increased and 45 proteins decreased in abundance (Figure 2B, Document S2). The changes observed with the WT strain upon CP stress are virtually identical with those obtained in a pairwise comparison of the CP-stressed Δ*zigA* strain vs untreated WT cells (Figure 2C–D). This reveals that the cellular impact of CP is not appreciably impacted by the absence of ZigA, which as a Zur target, reaches high intracellular levels (≈400 molecules per cell) only under conditions of CP-stress (Figure S2; Table 1; Document S2).[27,33]

Examination of the proteins that display increased abundance under CP stress is consistent with the pronounced Zn- and Fe-starvation phenotype reported previously,[33] as evidenced by the large number of proteins (26% of the total) that are components of the ferric uptake regulator (Fur) and Zur regulons (Table 1; Figure 2E). For example, the Fur-regulated enzymes used to synthesize the major mixed imidazole-catecholate Fe(III) siderophore acinetobactin (Figure S3A) (BasA-J), and the inner membrane transporter required to uptake Fe(III)-acinetobactin complexes (BauA-E),[68,69] as well as the Fe(III)-acinetobactin ferric reductase (BauF),[70] all become significantly more abundant in CP-stressed cells (Figure S3B). In addition, a TonB-dependent outer membrane-dependent receptor and ExbB/ExbD, which collectively energize the outer membrane for ferric-siderophore transport, are also more abundant under these conditions (Table 1; Figure S3). Proteins and enzymes required

for the biosynthesis and trafficking of the minor mixed catechol-hydroxymate Fe(III) siderophores, fimsbactin A and B (FbsA-E, FbsH-K, FbsM) as well as the baumannoferrin A and B, also become more abundant (Table 1; Figure S3). The Zur regulon is also highly induced by CP, and includes known Zur target genes encoding the low-Zn ribosomal protein paralog L31B (*rpmE2*), ZigA,[27] and components of the high affinity zinc uptake system, including ZnuA, ZnuD1 and the TonB/ExbB/ExbD system that is regulated by Zur (Table 1).[71,72]

Closer examination of the 45 proteins that display significantly decreased abundance under conditions of CP stress reveals a high enrichment (76% of the total) of known metal (Zn, Fe) or metallocofactor (Fe–S cluster) binding proteins and proteins involved in Fe–S protein biogenesis, including the cysteine desulfurase IscS, and the Fe–S assembly scaffold protein IscU (Table 2; Figure 2E). Fur itself is decreased by ≈3-fold, which is consistent with increased expression of the Fur regulon under these conditions (Table 1; Figure 2B). Proteins with decreased abundance include the large ribosomal protein L31 (encoded by *rpmE*), and a number of cell abundant, cytoplasmic [4Fe-4S] proteins (see Discussion), including the citric acid cycle housekeeping enzymes aconitase B (AcnB) and the class I fumarase (FumA), as well as a functionally uncharacterized, canonical Zn-dependent alcohol dehydrogenase. In fact, all four of these proteins are reciprocally regulated, in which a companion "low-metal paralog"[56] encoded by another gene displays increased abundance under conditions of CP-stress (Figure 2F–I). Biochemical experiments validate this aconitase switch as we find that low-metal induced paralog AcnA activity is completely refractory to chelator (EDTA) challenge in contrast to the housekeeping enzyme, AcnB (Figure 3A; Figure S4); these findings mirror what was found in *E. coli*, which in that work was traced to a weaker Fe-binding affinity.[73] The enhanced expression of a "back-up" aconitase A (*acnA*) has not been previously reported in *A. baumannii*, and could be regulated post-transcriptionally, as recently described in *Staphylococcus aureus*.[55] The reciprocal transcriptional regulation of the class I fumarase and Fe-independent class II fumarase, FumC, was previously noted under conditions of iron starvation in *A. baumannii* ATCC 17978,[74] as has the reciprocal transcription of L31 vs the Zur-regulated low-Zn paralog L31B (encoded by *rpmE2*).[33] In addition to these enzymes, two cofactor-synthesizing [4Fe-4S] enzymes, biotin synthase and lipoyl synthase, and a Zn-dependent carbonic anhydrase (MtcA2) also decrease in abundance (Table 2). Two other Zn-requiring methyltransferases involved in methionine synthesis (MetE) or homocysteine catabolism (MmnE) become less abundant upon CP-stress, as does the Zn-utilizing enzyme histidine ammonia lyase (HutH), previously tied to the CP-stress response (Table 2).[27]

CP-stressed cells also show significant reduction in Fe–S-cluster-containing membrane proteins including NuoE, NuoF and NuoG, key components of respiratory complex I, the NADH-ubiquinone oxidoreductase, which allows NADH-carried electrons to enter the electron transfer chain (ETC) (Table 2). In addition, comparable decreases in abundance are observed for respiratory complex II subunits that make up succinate dehydrogenase-ubiquinone oxidoreductase, the ETC entry point for $FADH_2$-derived electrons (Table 2). These findings again mirror results obtained from *E. coli*, where Fe-starvation leads to decreased abundance of components of the respiratory complexes I and II.[75] Both activities are significantly decreased in CP-stressed cells (Figure 3B–C; Figure S5) (see below). In

summary, we conclude that at least some fraction of the metalloproteome is destabilized and thus subject to increased turnover. This might be exacerbated by undermetalation of the essential Zn site II in the protein chaperone DnaJ, which would reduce the ability of cells to rescue misfolded proteins (discussed below). Finally, although cell-associated Mn levels are are also decreased slightly in CP-stressed cells (Figure S1B), increased cell abundance of the MumR-regulated manganese transporter MumT, a hallmark of Mn starvation, was not observed in the CP-stressed proteome (Document S2).[29] Two enzymes, including a Mn(II)-requiring superoxide dismutase (SodB) and a metal-binding cupin of unknown cofactor specificity do become decreased in cell abundance upon CP-stress.

Changes in Cysteine Reactivity across the Proteome.

We next determined the abundance-corrected changes in Cys reactivity across the proteome (Figure 4; Table 3; Table S2). Of the 2645 total unique quantified Cys-containing peptides, 150 unique Cys increase and 67 unique Cys decrease in net reactivity (≥2-fold; $\chi^2 \geq 9$) in WT *A. baumannii* stressed with CP (Figure 4A; Document S2). Once again, it is difficult to broadly differentiate the CP-treated WT from CP-treated Δ*zigA* cells (Figure 4B–C), with the changes in Cys reactivity very nearly identical in the two strain backgrounds (Table 3). In no case did we see a large increase in reactivity of a metal-coordinating Cys only in the Δ*zigA* strain, as might be expected for a ZigA metallochaperone client.[3,76] This suggests that if a high abundance client exists for ZigA, it likely involves a metal-coordination site that lacks Cys ligation, or the relevant Cys-containing peptide was not detectable in these experiments.

We next carried out a statistical analysis to determine the fraction of the Zn and Fe–S-cluster proteome being probed in this experiment (Figure 4D–E). Figure 4D shows that of the 106 Zn metalloproteins detected in this experiment, 31 harbor a Cys in the first coordination shell (Figure 4D, Table S2). Of these 31 proteins, 22 (76%) display a 2-fold or greater increase in reactivity with a chi-squared greater than 9, indicative of loss of the metal cofactor (Figure 4D). To probe the relationship between relative protein abundance and undermetalation, we performed label-free proteomics on soluble cell lysates of unstressed WT, and ranked proteins according to their fractional intensities[77,78] (Document S3) and highlighted those that were undermetalated in our chemoproteomics data sets (Figure 5A). These 22 Zn proteins in CP-treated cells are present at a median cell abundance that is comparable to all detected proteins and detected Zn enzymes (Figures 5B–C). Interestingly, the median abundance of these 22 undermetalated enzymes is slightly lower than from the seven Zn enzymes that show no increase in fractional occupancy of the metal site (Figure 5D). These data show that it is not uniquely the most abundant Zn enzymes in unstressed cells that become undermetalated in CP-stressed cells.

The opposite behavior seems to characterize the Fe–S proteome (Figure 5E–H). Out of the 43 Fe–S cluster proteins detected, 26 (60%) had a corresponding Cys-containing peptides that was localized to the first Fe–S cofactor coordination shell (Figure 4E). Only seven of these proteins are undermetalated by more than 2-fold (Figure 4E), and these enzymes appear higher in median cell abundance than those Fe–S cluster coordination sites that do not reach this significance threshold for a change in reactivity in the cell (Figure 5E–G).

This is in direct contrast with that of the Zn metalloproteome (Figure 5A–C). Further, all seven enzymes that are severely undermetalated are present at lower levels in chronically CP-stressed cells which suggests that the Fe–S proteome might be subject to turnover when not fully metalated (Table 2), *i.e.*, a global Fe-sparing response.[79] This is not true of the undermetalated Zn proteome, with just four of the 22 on this list of "destabilized" Zn metalloproteins including L31, which may constitute the bulk of the Zn-mobilization response.[80] Finally, the median cell abundance of these seven undermetalated Fe–S cluster enzymes in unstressed *A. baumannii* trends toward higher levels relative to those proteins that show no increase in fractional occupancy of the metal site (Figure 5H); this is also in contrast to the Zn proteome (Figure 5D). This analysis suggests the interesting finding that the response of the Zn proteome to decreased cell-associated Zn is distinct from that of the behavior of the Fe–S cluster proteome, which reflects no difference in total cell-associated Fe (Figure S1B).

Just below the 2-fold increase in Cys reactivity cutoff, are several other metalloproteins of interest (Table S1). These include IscU (C37), the only known Fe–S cluster assembly scaffold protein ($\log_2 = 0.64$) which becomes ≈2-fold more reactive in Δ*zigA* cells; IscU is also lower in cellular abundance (Table 2). In addition, the cysteine desulfurase IscS that functions upstream of IscU[81] is also reduced in cell abundance under conditions of CP-stress (Table 2). These findings suggest a negative impact on Fe–S biogenesis under these conditions. In addition, a 4Fe-4S dicluster domain-containing (ferredoxin-like) enzyme annotated as RnfB of unknown function is also substantially undermetalated under these conditions ($\log_2 = 0.94$). This is in contrast to two other ferredoxins, WrbA and FdxB, that are not substantially impacted by CP stress (Document S2). Another site of interest is C92 ($\log_2 = 0.93$) of peptide deformylase (PDF), an essential mononuclear His_2-Cys-H_2O Fe(II) enzyme[82] that cotranslationally cleaves the *N*-formyl group of the initiator formyl-Met of the nascent chain, the first step in the N-terminal Met excision pathway. PDF remains a *bona fide* antimicrobial drug target in many bacteria, including recent work in *A. baumannii*,[83] and oxidation or overoxidation of the Fe(II)-coordinating Cys leads to inactivation of the enzyme in *Salmonella enterica*.[82,84]

Undermetalation of the Fe–S Proteome, Cofactor Biosynthesis and Energy Generation.

One subset of enzymes not previously discussed that is affected by CP-mediated Fe starvation is the abundant Fe–S cluster proteins associated with a) biosynthesis of cofactors utilized by the energy-generating TCA cycle enzymes (biotin ligase, lipoate synthase), b) enzymes of the TCA cycle itself (aconitase, fumarase and succinate dehydrogenase), c) enzymes for CO_2 fixation (MtcA2), and d) subunits of respiratory complexes I and II, which utilize $FADH_2$ and NADH, respectively, as a source of electrons to power the membrane potential and ATP synthesis (Figure 6). We find significantly reduced specific activities for both respiratory complexes I and II (Figure 3B–C; Figure S5), derived from reduced protein levels, and a significantly reduced metal content in what actually remains in the membrane (Tables 2–3; Table S1). Thus, CP-stress appears to result in significantly fewer functional respiratory complexes in the plasma membrane.

Enzymes in Other Metabolic Pathways That Are Negatively Impacted by CP Stress.

Metalloproteins that are undermetalated (Table 3; Table S1) are associated with disparate cellular processes, and a number of these Zn enzymes are associated with GTP metabolism (Figure S6). The first two enzymes of the "lower" arm of the flavin biosynthesis pathway are catalyzed by the consecutive action of two Zn enzymes, GTP cyclohydrolase II (RibA) and $NADP^+$-dependent diaminohydroxyphospho-ribosylaminopyrimidine deaminase (RibD).[33] C55 in RibA ($log_2 = 0.90$) and C88 in RibD ($log_2 = 2.72$) are significantly undermetalated, with RibD among the most profoundly impacted Zn enzymes in the cell (Table 3). These findings are consistent with previous work that showed that *A. baumannii* employs an alternative 3,4-dihydroxy-2-butanone 4-phosphate synthase (DHBPS; RibBX) that catalyzes the first step of the "upper" arm of flavin biosynthesis pathway in an effort to maintain cellular flavin levels.[33] These data taken together suggest that CP-stress negatively impacts flavin biosynthesis with an important bottleneck in the sequential activities of RibA and RibD that occurs specifically as a result of undermetalation.

GTP is also the substrate for the Zn-enzyme GTP cyclohydrolase I (FolE) which makes the intermediate H_2–NTP, a metabolic branchpoint in folate and the queuosine (Q)-tRNA biosynthesis pathways.[36] A second metalloenzyme QueD2 (6-carboxy-5,6,7,8-tetrahydropterin (CPH_4) synthase) catalyzes the rate-determining step in Q-tRNA biosynthesis. Another Zn enzyme QueC, 7-deazo-7-deasaguanine synthase functions in the third step of the Q-tRNA biosynthesis pathway. FolE (C144), QueD2 (C18 from the inhibitory site 2[36]) and QueC (C190) are undermetalated, which pinpoints the sites of enzyme failure in cellular attempts to prioritize this pathway (Figure S6). These observations provide a molecular explanation for the previous finding that CP compromises flux through the Q-tRNA pathway.[36]

DISCUSSION

In the work presented here, we employ a change in the reactivity of the metal-ligating cysteines in metalloproteins to pinpoint for the first time across any bacterial proteome the impact of CP stress on the metal occupancy of the Cys metalloproteome. We observe significant and widespread undermetalation that potentially impacts many foundational cellular processes, from energy metabolism (Figures 3, 6; Figure S5) to GTP catabolism (Figure S6) to protein biosynthesis and homeostasis (Figures S7–S8). We take advantage of the fact that chronic CP-stress induces a significant Zn- and Fe-starvation regulatory response under our growth conditions, thus providing a means to evaluate and compare the integrity of the Zn and Fe–S proteomes in the same cells under the same stress conditions. We find that cellular Fe deficiency does not strongly track with reduced total cell-associated Fe under these conditions (Figure S1); this is also true in previously published work.[33] This suggests a marked change in cellular Fe-speciation that Fur senses as Fe starvation; indeed, reduced occupancy and decreased levels of cell-abundant Fe–S cluster enzymes (under metal-replete conditions) is direct evidence of a pronounced perturbation of Fe-speciation in CP-stressed cells, which is effectively Fe-sparing (Figure 5). Remarkably, the cellular fate of that spared Fe is currently unknown, but it is clearly not broadly bioavailable. Several possibilities exist, including the presence of a bacterioferritin that has lost the ability to

mobilize Fe(II) under these conditions,[85] or an as yet undiscovered Fe-storing encapsulin[86] distinct from the sulfur-storing encapsulin that is not detectable in CP-stressed *A. baumannii* proteomes.[87]

The molecular function of the candidate metallochaperone ZigA during adaptation to infected host-mediated nutritional immunity[27,33] is difficult to assess from the experiments shown here. The quantitative protein abundance data show no significant differences in the global proteome upon ZigA deletion; similarly, chemoproteomics reveal minimal changes in the net cysteine reactivity across the peptides detected, with the possible exception of several ribosomal proteins, none of which are metalloproteins. Given the anticipated functional similarities between ZigA and two previously characterized Zn metallochaperones, vertebrate Zng1 and *A. baumannii* MigC,[3,76,88,89] coupled to the fact that Zn binding to the conserved Cys-x-Cys-Cys motif strongly stimulates GTPase activity,[27,35] we would have expected to observe an increase in the reactivity of a Zn-coordinating cysteine(s) within a ZigA client protein(s). Therefore, the absence of such a finding is surprising. One possibility is that ZigA delivers metal to a non-Cys coordination site; alternatively, ZigA may simply interact with an as yet unidentified protein partner(s) in a guanine nucleotide- and/or Zn-regulated fashion, to an interface that lacks cysteines. Clearly, other approaches will have to be taken to identify a ZigA regulatory partner. One such approach would be to globally profile histidine reactivity in CP-stressed WT vs Δ*zigA* cells, which may well provide significantly deeper coverage specifically of the zinc metalloproteome and thus the functional role of ZigA.[90]

In general, undermetalation of the Zn proteome appears more nuanced than that of the Fe–S cluster proteome, and encompasses enzymes and proteins that vary significantly in their relative cell abundance (Figure 5). In an effort to identify a structural feature that might predispose a Cys-Zn proteome site to metal loss under conditions of CP-induced metal limitation, we further analyzed our undermetalated Zn proteome sites and compared these sites to those that did not meet our statistical criteria for significant loss of metal as well as to Cys proteome. Zn-sites rich in cysteine sulfur ligation might be anticipated to form slightly higher affinity complexes compared to those consisting of lighter N/O atoms;[91] in this case, tetrathiolate (S_4) sites might exhibit higher resistance to metal loss. We find that fraction of undermetalated S_4 Zn-sites matches their estimated percentage in the Cys-Zn proteome (≈50%). Alternatively, the proximity of Zn ligands in the primary structure may also impact Zn loss if cotranslational metal insertion in the ribosome exit tunnel contributes significantly to metalation of the Zn-Cys metalloproteome. If we consider all four Zn ligands as being “close” in the primary structure as within ≈40 residues in the primary structure,[92] 60% of the undermetalated sites we observe here meet this definition; however, this is close to the approximate number of sites in the Zn-Cys proteome that are close in the primary structure. Therefore, we cannot easily identify a specific structural feature in these coordination sites that might distinguish them from Zn-sites that are unaffected by CP-stress. It will be necessary to broadly investigate the thermodynamics of metal binding, as well as the kinetics of metal dissociation[36] to investigate this further. One exciting possible outcome of future studies that leverage these findings is that those Zn proteins that exhibit reduced metal occupancy simply have lower Zn affinities relative to those that are not similarly

affected; such a result would be fully consistent with the set-point model of metal occupancy and further allow an estimate of bioavailable Zn in CP-stressed *A. baumannii* cells.[42]

We also find that the steady-state levels of these undermetalated Zn enzymes are not severely impacted, with the exception of ribosomal protein L31. L31 is expected to have very little structure once dissociated from the ribosome, which will be exacerbated by the loss of the bound Zn, making L31 an excellent substrate for cellular proteases (Figure 2H). Only three other Zn enzymes are characterized by significantly decreased abundance coupled to reduced metal occupancy, including the β-class carbonic anhydrase and two of the five undermetalated tRNA synthetases, isoleucine- and cysteinet-RNA synthetases. This general response of the Zn proteome to metal starvation contrasts with those seven undermetalated enzymes of the Fe–S proteome, all of which are reduced in steady-state abundance, relative to those that retain their Fe–S clusters. This suggests that the metalation status of the Fe–S proteome is more strongly connected to protein homeostasis (biosynthesis, degradation and post-translational modification) than is the Zn proteome, which appears largely uncoupled from proteostasis mechanisms. The reasons for this are unknown, but one possibility is that reduced Zn occupancy fails to engage an unfolded protein response, which might in turn lead to enhanced degradation and cellular turnover of these apo-enzymes relative to the Fe–S proteome. This is broadly consistent with the set-point model, in that the Cys-Zn metalloproteome exists as a superposition of nonmetalated and metalated pairs of enzymes, the metalation status of which appears broadly responsive to the bioavailable Zn pool.[42] In this case, a careful analysis of the zinc binding affinities of all 29 Cys-Zn enzymes might define the Zn set-point for chronically CP-stressed cells.

The work presented here, although not thoroughly investigated, suggests that CP-stress has many hallmarks of nutritional stress while at the same time potentially disarming the ability of cells to fully engage the stringent response as a consequence of undermetalation of key players in this process. One metabolic fate of GTP is its hyperphosphorylation to the alarmone (p)ppGpp by GTP pyrophosphatase (RelA) (Figure S6) as part of the stringent response to general nutrient starvation. RelA associates with ribosomes in an unacylated A-site tRNA conformation and contains a C-terminal regulatory Zn-finger domain (ZFD) that has been shown to stabilize the interaction with the ribosome; mutagenesis of a key Cys in the ZFD (equivalent to our hypermodified C662 in *A. baumannii* RelA) is expected to impact association with the ribosome, which would lead to a reduced stability in cells.[93,93,94] This undermetalation of RelA in CP-stressed cells is read out by enhanced reactivity of C662 thus potentially undermining cellular efforts to mount the stringent response (Figure S6).

Indeed, as found earlier,[33] CP-stressed cells have a lower complement of ribosomes (≈60% of untreated cells) (Figure S7A); these cells are also strongly enriched in two ribosome hibernation factors, RaiA and Hpf (hibernation promoting factor), each of which binds to the 70S ribosome and inactivates translation via distinct mechanisms (Table 2; Figure S7B).[95,96] 70S ribosomes purified from CP-stressed cultures appear enriched for Hpf; in addition, these 70S particles are also enriched for small protein B (SmpB), despite no change in its cellular abundance (Figure S7A; Document S2). SmpB, in complex with alanyl-charged tm (transfer-messenger) RNA mediates *trans*-translation, the major rescue process for stalled

ribosomes that result from a defective mRNA (“non-stop”), or an empty (deacylated) A-site (“no-go”) that results from amino acid limitation (Figure S7B), in a process that is functionally parallel to (p)ppGpp synthesis.[97,98] Interestingly, Ala-tRNA synthetase is one of five highly cell abundant tRNA synthetases that is undermetalated in CP-stressed cells, which may in turn compromise this rescue process (Figure S7C). Thus, 70S ribosomes from CP-stressed *A. baumannii* cells are not only lower in number, but those that are present may be in various states of maturation[99,100] or functionality. These findings mirror those in mycobacteria where Zn depletion induces ribosome hibernation.[60]

The stringent response is employed by bacteria to combat nutrient deprivation. Mechanisms that are used to globally remodel the proteome, including the selected use of tRNA modifications (Figures S6–S7), proteostasis, sRNA regulation and RNA processing (Figure S8), may well be compromised by significant undermetalation of key enzymes that maintain these processes. These enzymes include DnaJ, a housekeeping hsp40-class molecular cochaperone that helps to maintain the integrity of the proteome (Figure S8A), and which is among the topmost undermetalated proteins in cells (Table 3); further, the Cys in DnaJ that reports on metalation status (C167) is a ligand to a zinc site II that is essential for the interaction with DnaK.[101] Others include a Cys residue in the SecY-interacting motif of SecA, an ATPase motor protein that powers movement of unfolded proteins destined for the periplasm or the extracellular space through the SecYEG channel,[102] and the Cys residues of the “Zn-link” motif of RNase E,[103] an essential component of the RNA degradasome[104] intimately involved in sRNA-mediated regulation of gene expression (Figure S8B).

If undermetalation of the above-indicated Zn enzymes (Figures S6–S8) even partially impacts their cellular activities, this might be expected to induce a broad remodeling of the proteome. These perturbations might in turn be expected to induce a “knock-on” effect akin to Q-tRNA and ms^2i^6A-tRNA modification (which requires the 4Fe-4S cluster-containing methylthiotransferase MiaB[105] that is undermetalated in these cells; see Table 3) in transfer-RNA pools, and in the integrity of tRNA charging itself (Figure S7) under conditions of nutritional stress.[106] In fact, some fraction of the proteome that increases in cellular abundance in the “other” category (Figure 2E) may be attributed to indirect effects like these. Additional experiments, including a comprehensive analysis of CP-stressed metalloproteome and the metabolome will provide deeper insights into metabolic rewiring in CP-stressed cells. This work is underway.

MATERIALS AND METHODS

Chemoproteomics and Mass Spectrometry.

Generation of A. baumannii Lysates. Calprotectin was expressed in *E. coli* and purified as previously reported.[12,16] Wild-type (WT) and Δ*zigA A. baumannii* cells were cultured overnight as biological duplicate in a standard Tris-LB medium used previously.[33] The overnight cultures were diluted 1:50 into 2 mL Tris-LB media and given 1.5 h to recover at 37 °C. Final cultures were prepared in 50 mL total volume of fresh media in a sterile 250 mL Erlenmeyer flask and grown with vigorous aeration until an OD_{600} of 0.370 was reached in the absence or presence of 300 μg/mL CP. The cells were harvested by centrifugation at 4000*g* at 4°C for 15 min, washed in 1 mL of 1 x PBS pH 7.4, and

then immediately frozen at − 80 °C until further analysis. Cell pellets were thawed and resuspended in 500 μL lysis buffer (PBS, pH 7.4 + 0.1% NP-40), lysed by three rounds of sonication (10 × 1 s pulses, 85% amplitude) and centrifuged at 10,000*g* at 4°C for 15 min to generate clarified lysates. Protein concentration was determined by Bradford assay (BioRad) and lysates were diluted to a concentration of 1 mg mL^{-1} with lysis buffer.

SP3 Purification and Trypsin Digestion. Samples were prepared in biological duplicate for each study condition, for a total of six (6) study channels (2x untreated WT, 2x CP (300 μg/mL)-stressed WT, and 2x CP-stressed Δ*zigA* cells). For each channel, 50 μL of lysate (50 μg, 1 mg mL^{-1}) was portioned into a low-bind 1.5 mL Eppendorf tube with 50 μL of lysis buffer. Each channel was treated with of 5 μL of 10 mM iodoacetamide-desthiobiotin (DBIA) for 1 h at RT in the dark with intermittent vortexing every 15 min. After DBIA labeling, 15 μL of magnetic SP3 beads (1:1 hydrophobic:hydrophilic, 50 mg mL^{-1}) and 150 μL of 20 mM DTT in 98% ethanol were added to each channel followed by 10 min incubation with rotation. The beads were pelleted using a magnetic Eppendorf rack and the supernatant removed. The beads were washed once with 500 μL of 80% ethanol, followed by the addition of 100 μL of 20 mM iodoacetamide in lysis buffer and 30 min incubation with rotation in the dark. Next, 200 μL of 20 mM DTT in 98% ethanol was added with another 10 min incubation with rotation in the dark. Following pelleting and removal of the supernatant, the beads were washed twice with 500 μL of 80% ethanol. The washed beads for each channel were then incubated overnight with rotation at RT in 150 μL of 200 mM EPPS buffer, 1 mM calcium chloride, and 1.5 μg sequencing grade modified trypsin.

TMT-Labeling. After trypsin digestion, 69 μL of acetonitrile and 6 μL of the corresponding TMT-tag (20 μg/μL in acetonitrile) was added to each of the 6 channels and the reaction was allowed to incubate at RT with rotation for 60 min. The reaction was then quenched by the addition of 35 μL of 5% hydroxylamine in water, followed by incubation at RT with rotation for 10 min. The 6 channels were combined into one low-bind 2 mL Eppendorf tube and dried on a speed-vac. The combined peptide/bead sample was then resuspended in 500 μL of 10% formic acid in water and the supernatant removed from the beads on a magnetic rack. The supernatant was then desalted with a 360 mg Sep-Pak per manufacturer's directions. The peptide sample was eluted in a final volume of ≈1 mL into a low-bind 2 mL Eppendorf tube, with 250 μL of this elution transferred to a second low-bind 2 mL Eppendorf tube for subsequent off-line fractionation (see below "Off-line fractionation⋯") and protein abundance analysis. The remaining ≈750 μL in the first Eppendorf tube was subjected to enrichment on streptavidin beads (see below "Streptavidin enrichment⋯") and analyzed for cysteine reactivity. Both of the samples were dried to completeness overnight on a speed-vac.

Streptavidin Enrichment for Cysteine Reactivity Analysis. The combined sample (first Eppendorf tube from the "TMT labeling" section) was resuspended in 1 mL of 100 mM HEPES, pH 7.4. Addition of 50 μL of prewashed high-capacity streptavidin agarose beads as a 50% slurry to the samples was followed by incubation for 3 h with rotation at RT. The bead mixture was transferred to a Ultrafree-MC centrifugal filter (hydrophilic PTFE, 0.22 μm pore size) and centrifuged at 800xg for 30 s to remove the supernatant. The beads

were subsequently washed with 3 × 300 μL of 100 mM HEPES, pH 7.4, with 0.05% NP-40, 3 × 300 μL of 100 mM HEPES, pH 7.4, and 3 × 300 μL of water. DBIA-labeled peptides were eluted from the beads with 3 × 300 μL additions of 80% acetonitrile, 0.1% formic acid (1 × 20 min incubation at RT, 1 × 10 min at RT, and 1 × 10 min at 72 °C). The combined elution was dried on a speed-vac, before being resuspended in 25 μL low pH buffer A (95% H_2O, 5% acetonitrile, 0.1% formic acid). Peptide concentration was determined by quantitative peptide assay kit (Pierce) as per the manufacturer's instructions and the sample diluted to 100 ng/μL with low pH buffer A.

Offline Fractionation for Protein Abundance Analysis. The combined sample (second Eppendorf tube from the "TMT labeling" section) was resuspended in 500 μL high pH buffer A (95% H_2O, 5% acetonitrile, 10 mM ammonium bicarbonate) and loaded onto a manual injection loop connected to an Agilent 1100 Series HPLC. Peptides were separated on a 25 cm Agilent Extend-C18 column using a 60 min gradient from 20 to 35% high pH buffer B (10% H_2O, 90% acetonitrile, 10 mM ammonium bicarbonate). Fractions were collected using a Gilson FC203B fraction collector into a 96 deep-well plate (0.6 min/well). Subsequent concatenation of every sixth well resulted in six pooled fractions that were dried by speed-vac and then resuspended in 50 μL of low pH buffer A. Peptide concentration was determined by quantitative peptide assay kit (Pierce) per manufacturer's instructions and each fraction was diluted to 100 ng/μL with low pH buffer A.

LC-MS/MS of Peptide Samples. Mass spectrometry-based proteomic analysis of each sample/fraction was performed as technical replicates, triplicate for cysteine reactivity and duplicate for protein abundance. LC-MS/MS was performed on an Orbitrap Exploris 240 mass spectrometer running Xcalibur v4.4 (Thermo Scientific) coupled to a Dionex Ultimate 3000 RSLCnano system. Each sample (5 μL, 500 ng peptide) was injected directly onto an Acclaim PepMap 100 loading column. Peptides were eluted onto an Acclaim PepMap RSLC and separated with a 2 h gradient from 5% to 25% of Buffer B (20% H_2O, 80% MeCN, 0.1% formic acid) in Buffer A (100% H_2O, 0.1% formic acid) at a flow rate of 0.3 μL/min. The spray voltage was set to 2.1 kV. One full MS1 scan (120,000 resolution, 350–1800 *m*/*z*, RF lens 65%, AGC target 300%, automatic maximum injection time, profile mode) was obtained every 2 s with dynamic exclusion (repeat count 1, duration 20 s), isotopic exclusion (assigned), and apex detection (30% desired apex window) enabled. A variable number of MS2 scans (30,000 resolution) were obtained between each MS1 scan based on the highest precursor masses, filtered for monoisotopic peak determination, intensity (5E4), and charge state (2–6). MS2 analysis consisted of the isolation of precursor ions (isolation window 0.7 *m*/*z*) followed by higher-energy collision dissociation (HCD, collision energy 36%).

Database Search and Quantification. The tandem MS data was analyzed by the Thermo Proteome Discoverer V2.4 software package and searched using the SequestHT and Percolator algorithms against a UniprotKB database (www.uniprot.org) of the *A. baumannii* proteome (UP000072389–02/15/2024). Trypsin was specified as the protease with a maximum of two missed cleavages. Peptide precursor mass tolerance was set to 10 ppm with a fragment mass tolerance of 0.02 Da. The false discovery rate (FDR) for peptide identification was set to 1%. Oxidation of methionine (+15.995) as well as

acetylation (+42.011) and/or methionine-loss (+131.040) of the protein N-terminus were set as dynamic modifications and TMT-tag labeling (+229.163) of lysine residues and peptide N-termini were set as static modifications. For protein abundance analysis, cysteine alkylation (+57.021) was set as a static modification, while for cysteine reactivity analysis, cysteine alkylation (+57.021) and DBIA labeling (+296.185) were both set as dynamic modifications. For TMT-based quantification, a centroid tolerance of 20 ppm was applied for integration, with a coisolation threshold of 50% and an average reporter signal-to-noise threshold of 10. Normalization of each channel was applied based on the total peptide signal of all peptides. Peptide ratio quantification was based on S/N values, while protein ratios were calculated from grouped abundances excluding cysteine containing peptides. P-values were calculated by ANOVA of individual peptide or protein abundances. Annotation of cysteine function was generated from the Uniprot Protein Knowledgebase (UniProtKB).

Fe–S Cluster and Zn Proteome Predictions.

For the prediction of the Fe–S proteome, we used the MetalPredator server[62] to scan the *A. baumannii* ATCC17978-VU proteome with default parameters. This resulted in a list of 92 putative Fe–S cluster proteins (Document S1). For the prediction of the Zn proteome, we used the approaches previously employed,[33,62] creating two libraries of Hidden Markov Model (HMM) profiles, one based on known Zn-binding Pfam domains, and another based on specific Zn-binding structural motifs. The former library was created by combining domains with a known 3D structure and domains without a known structure but annotated as Zn-binding. The latter library was obtained by fragmenting Zn-binding sites from existing protein structures, while excluding nonphysiological sites. We then used these two libraries to scan the *A. baumannii* ATCC 17978-VU proteome with the hmmscan tool,[107] filtering out proteins matching HMM profiles that did not conserve the Zn-binding residues. This procedure yielded a list of 203 putative Zn proteins, which was integrated with data from the UniProt database resulting in a final list of 225 putative Zn proteins (Document S1).

Multireaction Monitoring for Quantitation of ZigA.

Generation of ^{15}N-ZigA Spiked A. baumannii Lysates. Pipette stabs from a frozen glycerol stock of ATCC 17978-VU were transferred into triplicate cultures containing 1 mL Tris-LB and grown with shaking at 37 °C for 16 h. Overnight cultures were diluted 1:50 into 1 mL fresh media and given 1 h to recover in the 37 °C incubator. Recovery cultures were finally diluted 1:500 into 10 mL Tris-LB with and without 300 μg/mL calprotectin. Cells were collected once cultures reached an OD600 of 0.4, washed with 1 mL wash buffer (25 mM Tris pH 7.5, 100 mM NaCl), and stored at − 80 °C until use. Pellets were resuspended in 600 μL lysis buffer (25 mM HEPES pH 7.4, 150 mM NaCl, 2.5 mM TCEP, EDTA-free protease inhibitor) and transferred to lysing matrix B tubes, which were then lysed on an Omni Bead Ruptor 12 homogenizer by performing a standard lysis protocol (6 m/s, 3 min on, 1.5 min off, 30 s total) twice. Lysates were centrifuged at 20,000*g* for 10 min and the supernatants were decanted into clean 1.5 mL Eppendorf tubes. This step was repeated in order to remove any residual beads and insoluble material. ^{15}N-*Ab*ZigA was spiked into each lysate replicate with the appropriate amount added based on preliminary lysate analysis and the standard curve that was generated from ratiometric standards. Total protein content in each sample was then measured by Bradford assay.

Preparation of $^{15}N/^{14}N$-AbZigA Ratiometric Standards. Uniformly labeled ^{15}N- and unlabeled-*Ab*ZigA were purified as previously described.[35] Seven quantitation standards were generated by mixing calculated mass ratios of ^{15}N:^{14}N protein in triplicate ranging from 0 to 1.0. The normalized ^{15}N:^{14}N mass ratios were plotted against their normalized ^{15}N:^{14}N signal ratios for multiple tryptic peptides to generate standard curves.

Trypsin Digest and Peptide Desalting. Twenty μg of protein (standard or lysate) was transferred to a clean Eppendorf tube and dried down using a SpeedVac concentrator. Pellets were resuspended in 100 μL 8 M urea and 100 mM ammonium bicarbonate solution. Then, 2 μL 0.5 M TCEP and 10 μL 200 mM iodoacetamide was added to each sample and stored for 1 h in the dark at RT for subsequent reduction and alkylation. Protein precipitation was initiated by adding 25 μL of trichloroacetic acid and continued for 1 h at − 20 °C. Samples were pelleted in a SpeedVac by centrifugation for 20 min at 20,000*g*, and the supernatant was carefully removed. Proteins were washed with 500 μL of cold acetone, and the samples were dried by SpeedVac concentration. Trypsin digestion was initiated after dissolving the pellets in 100 μL 1 M urea and 100 mM ammonium bicarbonate containing 2 ng/μL sequencing-grade trypsin. Resuspensions were incubated for >16 h in a shaking incubator set to 37 °C. Five μL 10% trifluoroacetic acid was then transferred to each digest to quench the reaction and precipitate the resulting peptides. A desalting step was performed using C18 Zip Tips and the peptides were eluted in 25 μL 50% acetonitrile in water and 0.1% trifluoroacetic acid.

LC-MS/MS Proteomic Analysis and Calculations. Samples were analyzed on an Orbitrap Fusion Lumos Tribrid mass spectrometer coupled to an Easy-nanoLC 1200. Peptides were loaded onto an Acclaim PepMap 100 C18 trap column (75 μm x 2 cm, 100 Å) in 0.1% formic acid. The peptides were separated using an Acclaim PepMapTM 100 analytical column (75 μm x 25 cm, 100 Å) using an acetonitrile-based gradient (Solvent A:0% acetonitrile, 0.1% formic acid; Solvent B: 80% acetonitrile, 0.1% formic acid) at a flow rate of 300 nL/min. A 60 min gradient was implemented as follows: 0 min, 4% B; 0–53 min, 4–26% B; 53–55 min, 26–100% B; 55–60 min, 100% B followed by re-equilibration to 4% B. The electrospray ionization was carried out with a nanoESI source at a 260 °C capillary temperature and 1.8 kV spray voltage. The mass spectrometer was operated in data-dependent acquisition mode with mass range 400 to 2000 *m/z*. The precursor ions were selected for tandem mass (MS/MS) analysis in Orbitrap with 3 s cycle time using HCD at 35% collision energy. Intensity threshold was set at 2e5. The dynamic exclusion was set with a repeat count of 1 and exclusion duration of 60 s. The abundances of unlabeled and ^{15}N-labeled versions of peptides were manually determined using the Qual Browser program within Xcalibur.[15] N:^{14}N signal ratios of tryptic peptides from spiked lysates were plotted against their respective standard curves to determine the mass of ^{14}N-ZigA present. The final number of ZigA proteins per cell was calculated under the assumption that an OD600 of 1 = 8×10^8 cells.

Label-Free Proteomics Analysis of *A. baumannii* Soluble Cell Lysates.

Preparation of *Ab* lysates, along with downstream digestion and peptide desalting, followed the same procedures as previously described.[33] The LC-MS analysis was

conducted in a similar manner to the preceding section. The resulting data were searched against an *Acinetobacter baumannii* database (Uniprot UP000094982, 3,780 entries, with the database downloaded on 07/06/2017 from Uniprot) in Proteome Discoverer 2.5. Carbamidomethylation of cysteine residues was set as a fixed modification. Protein N-terminal acetylation, oxidation of methionine, protein N-terminal methionine loss, protein N-terminal methionine loss and acetylation, and pyroglutamine formation were set as variable modifications. A total of 3 variable modifications were allowed. Trypsin digestion specificity with two missed cleavage was allowed. The mass tolerance for precursor and fragment ions was set to 10 ppm and 0.05 Da, respectively. Peptides abundances were quantified using the Precursor Ions Quantifier node. Protein abundances were estimated from the three most abundant peptides from a given protein and those that were assigned with less than 3 unique peptides were filtered out of the ranked abundance analysis.

Preparation and Characterization of Fe–S Cluster-Loaded *Ab*AcnA and *Ab*AcnB.

Cloning, Induction, and Purification. A1S_0558 (AcnA) and A1S_2126–2128 (AcnB) were amplified from *A. baumannii* ATCC17978-VU genomic DNA and cloned into the pHis-parallel1 expression vector at the *Nco*I recognition site using isothermal assembly. Constructs were designed to include a 6X His-tag followed by a TEV cleavage sequence. The resulting plasmids were transformed into BL21(DE3) competent cells by heat shocking for 45 s at 42 °C. Surviving cells were selected on an LB agarose plate supplemented with 100 μg/mL ampicillin that was incubated at 37 °C overnight. Colonies were then picked, transferred to 1 L LB medium containing ampicillin, and grown at 37 °C while shaking vigorously. Once cultures reached an OD600 of 0.6–0.8, 1 mL of 1 mM isopropyl β-D-1-thiogalactopyranoside was added to induce heterologous expression. The temperature was then reduced to 18 °C and incubation continued overnight. Cultures were centrifuged (5,000*g*, 4 °C, 20 min), the pellets were resuspended in 40 mL lysis buffer (25 mM Tris pH 8.0, 500 mM NaCl, 2 mM TCEP, EDTA-free protease inhibitor), and then sonicated for 10 min (2 s on, 8 s off, 60% power) in an ice bath. Insoluble material and DNA were removed from lysates with addition of 10% polyethylenimine (PEI) and centrifugation (14,000*g*, 4 °C, 20 min). Recombinant AcnA or AcnB were then bound to a prepacked, pre-equilibrated 5 mL Ni-NTA HisTrap column connected to an AKTA liquid chromatography system. The column was washed thoroughly with Buffer A (25 mM Tris pH 8.0, 500 mM NaCl, 25 mM imidazole) before eluting with a 0–100% gradient to Buffer B (25 mM Tris pH 8.0, 500 mM NaCl, 1 M imidazole). Fractions containing the desired protein were pooled, concentrated, and finally injected onto a 120 mL Sephadex G75 in buffer (25 mM Tris pH 8.0, 150 mM NaCl, 1 mM EDTA, 2 mM TCEP) for additional purification. The resulting purified protein was buffer exchanged into chelex-treated metal-free buffer (25 mM HEPES pH 7.4, 150 mM NaCl, 2 mM TCEP) by dialysis to remove EDTA and stored at − 80 °C.

Loading Fe–S Clusters. Protocols to reconstitute Fe–S clusters into AcnA and AcnB were adapted from previous work.[108,109] All buffers and reagents were freshly prepared and degassed the same day. Thawed protein was transferred into an anaerobic chamber containing <1 ppm of O_2, and briefly buffer exchanged into degassed metal-free buffer. Following reduction with 10 mM DTT, 8-fold molar excess of Mohr's salt ($Fe(NH_4)_2(SO_4)_2{\cdot}6H_2O$) was added to the protein and the reaction was allowed to stand for

5 min. The same concentration of Na_2S was then introduced, and the solution was incubated for 1–2 h. A color change could be observed after 30 min, typically to red or brown. Excess Fe and Na_2S was removed after passing the samples through a PD-10 desalting column in the anaerobic chamber. An observable peak at ≈420 nm by UV–vis confirmed the presence of Fe–S clusters.

AcnA and AcnB Activity Assays. Activity assays were performed using the Abcam colorimetric aconitase kit (ab109712). Reactions were initiated by the addition of AcnA or AcnB (500 nM final conc.) into the supplied buffer containing excess isocitrate. Formation of the intermediate cis-aconitate from isocitrate was monitored as an increase in absorbance at 240 nm ($\varepsilon_{240\ nm}$ = 3.6 mM^{-1} cm^{-1}). For assays containing 300 μM EDTA, enzymes were preincubated with EDTA for 30 min prior to activity measurements. Calculated activities were background corrected.

Purification of Total Membrane Fractions from *A. baumannii*.

300 mL of *Ab* ± 300 μg/mL CP were grown in Tris-LB and cells collected as described above. Further purification of the membrane fraction closely followed published methods.[110] Briefly, cell pellets were resuspended in 12.5 mL of buffer A (0.5 M sucrose, 10 mM Tris, pH 7.5), 180 μL lysozyme was added from a freshly prepared 10 mg mL^{-1} stock and stirred on ice for 2 min. 12.5 mL of 1.5 mM EDTA was then added to the mixture and allowed to mix for 7 min before centrifugation at 11,000*g* for 10 min. The supernatant was decanted and the isolated pellet was resuspended in 5 mL buffer B (0.2 M sucrose, 10 mM Tris pH 7.5) containing EDTA-free protease inhibitor. The suspension was vigorously vortexed until homogeneous and aliquoted into six lysing matrix B tubes. Cells were lysed using an Omni Bead Ruptor 12 with the standard lysis protocol (30 s total, 3 s on, 2 min off, 6 m/s) performed twice at 4 °C. Lysates were centrifuged to clear cellular debris and pooled into Ti70 tubes, then diluted to the top with buffer B before ultracentrifugation at 184,500*g* for 6 h. The supernatant was carefully decanted and the remaining pellet was resuspended in 2 mL isolated membrane storage buffer (10 mM Tris-HCl, pH 7.5) by dounce homogenization. Protein concentrations were measured by Bradford assay, and total membrane fractions were stored at − 20 °C until further analysis.

NADH-Quinone Dehydrogenase and Succinate-Quinone Dehydrogenase Assays.

NADH-quinone dehydrogenase activity in purified *A. baumannii* membranes was measured by the conversion of NADH to NAD^+, observed by a decrease in absorbance at 340 nm ($\varepsilon_{340\ nm}$ = 6.22 mM^{-1} cm^{-1}). Reactions were initiated with the addition of 50 μg membrane protein into storage buffer containing 200 μM NADH and were monitored for 5 min or until the substrate was fully consumed. Calculated activities were background-corrected using reactions monitored without protein. Succinate-quinone dehydrogenase was assayed according to a published protocol.[111] Briefly, 10 μg of membrane protein was introduced into a mixture containing 400 μM phenazine methanosulfate (PMS), 100 μM succinate-2,6-dichlorophenolindophenol (DCPIP), and 5 mM sodium succinate in buffer. Reactions were monitored by a decrease in absorbance at 600 nm ($\varepsilon_{600\ nm}$ = 20.7 mM^{-1} cm^{-1}), indicating successful oxidation of succinate, subsequent electron transfer to the intermediate PMS, and

final reduction of DCPIP. Calculated activities were background corrected using reactions monitored without protein.

Purification of Ribosomes from Unstressed and CP-Stressed *A. baumannii*.

500 mL cultures of *Ab* ± 300 μg/mL CP were grown in Tris-LB as described above and cells collected, with tight-coupled ribosomes purified as described[112] and subjected to label-free quantitation as described above.

Supplementary Material

Refer to Web version on PubMed Central for supplementary material.

ACKNOWLEDGMENTS

We gratefully acknowledge support by the US National Institutes of Health grants R01 AI101171 (E. P. S, W. J. C. and D. P. G.), R35 GM118157 (D. P. G.), R01 AI127793 (W. J. C), and R35 GM134964 (E. W.) and US National Science Foundation (MCA 2122902 to P. V. C.). M. K. O. was supported by a graduate fellowship provided the Training Program in Quantitative and Chemical Biology (QCB) at Indiana Univerrsity (T32 GM131994).

REFERENCES

(1). Murray CJL; Ikuta KS; Sharara F; Moore C Global burden of bacterial antimicrobial resistance in 2019: A systematic analysis. Lancet 2022, 399, 629–655. [PubMed: 35065702]

(2). NIHR Global Health Research Unit on Genomic Surveillance of AMR. Whole-genome sequencing as part of national and international surveillance programmes for antimicrobial resistance: A roadmap. BMJ. Glob Health 2020, 5, No. e002244.

(3). Capdevila DA; Rondon JJ; Edmonds KA; Rocchio JS; Dujovne MV; Giedroc DP Bacterial Metallostasis: Metal Sensing, Metalloproteome Remodeling, and Metal Trafficking. Chem. Rev 2024, 124, 13574–13659. [PubMed: 39658019]

(4). Murdoch CC; Skaar EP Nutritional immunity: The battle for nutrient metals at the host-pathogen interface. Nat. Rev. Microbiol 2022, 20, 657–670. [PubMed: 35641670]

(5). Sheldon JR; Skaar EP Metals as phagocyte antimicrobial effectors. Curr. Opin Immunol 2019, 60, 1–9. [PubMed: 31063946]

(6). Jordan MR; Wang J; Capdevila DA; Giedroc DP Multi-metal nutrient restriction and crosstalk in metallostasis systems in microbial pathogens. Curr. Opin Microbiol 2020, 55, 17–25. [PubMed: 32062305]

(7). Lonergan ZR; Skaar EP Nutrient Zinc at the Host-Pathogen Interface. Trends Biochem. Sci 2019, 44, 1041–1056. [PubMed: 31326221]

(8). Weinberg ED Nutritional immunity. Host's attempt to withold iron from microbial invaders. JAMA 1975, 231, 39–41. [PubMed: 1243565]

(9). Weinberg ED Iron and susceptibility to infectious disease. Science 1974, 184, 952–956. [PubMed: 4596821]

(10). Corbin BD; Seeley EH; Raab A; Feldmann J; Miller MR; Torres VJ; Anderson KL; Dattilo BM; Dunman PM; Gerads R; Caprioli RM; Nacken W; Chazin WJ; Skaar EP Metal chelation and inhibition of bacterial growth in tissue abscesses. Science 2008, 319, 962–965. [PubMed: 18276893]

(11). Kehl-Fie TE; Skaar EP Nutritional immunity beyond iron: a role for manganese and zinc. Curr. Opin Chem. Biol 2010, 14, 218–224. [PubMed: 20015678]

(12). Kehl-Fie TE; Chitayat S; Hood MI; Damo S; Restrepo N; Garcia C; Munro KA; Chazin WJ; Skaar EP Nutrient metal sequestration by calprotectin inhibits bacterial superoxide defense, enhancing neutrophil killing of *Staphylococcus aureus*. Cell Host Microbe 2011, 10, 158–164. [PubMed: 21843872]

(13). Zygiel EM; Nelson CE; Brewer LK; Oglesby-Sherrouse AG; Nolan EM The human innate immune protein calprotectin induces iron starvation responses in Pseudomonas aeruginosa. J. Biol. Chem 2019, 294, 3549–3562. [PubMed: 30622135]

(14). Nakashige TG; Nolan EM Human calprotectin affects the redox speciation of iron. Metallomics 2017, 9, 1086–1095. [PubMed: 28561859]

(15). Zygiel EM; Nolan EM Transition Metal Sequestration by the Host-Defense Protein Calprotectin. Annu. Rev. Biochem 2018, 87, 621–643. [PubMed: 29925260]

(16). Damo SM; Kehl-Fie TE; Sugitani N; Holt ME; Rathi S; Murphy WJ; Zhang Y; Betz C; Hench L; Fritz G; Skaar EP; Chazin WJ Molecular basis for manganese sequestration by calprotectin and roles in the innate immune response to invading bacterial pathogens. Proc. Natl. Acad. Sci. U. S. A 2013, 110, 3841–3846. [PubMed: 23431180]

(17). Antelo GT; Vila AJ; Giedroc DP; Capdevila DA Molecular Evolution of Transition Metal Bioavailability at the Host-Pathogen Interface. Trends Microbiol 2021, 29, 441–457. [PubMed: 32951986]

(18). Cunden LS; Gaillard A; Nolan EM Calcium Ions Tune the Zinc-Sequestering Properties and Antimicrobial Activity of Human S100A12. Chem. Sci 2016, 7, 1338–1348. [PubMed: 26913170]

(19). Cunden LS; Nolan EM Bioinorganic Explorations of Zn(II) Sequestration by Human S100 Host-Defense Proteins. Biochemistry 2018, 57, 1673–1680. [PubMed: 29381858]

(20). Brophy MB; Hayden JA; Nolan EM Calcium ion gradients modulate the zinc affinity and antibacterial activity of human calprotectin. J. Am. Chem. Soc 2012, 134, 18089–100. [PubMed: 23082970]

(21). Besold AN; Gilston BA; Radin JN; Ramsoomair C; Culbertson EM; Li CX; Cormack BP; Chazin WJ; Kehl-Fie TE; Culotta VC Role of Calprotectin in Withholding Zinc and Copper from Candida albicans. Infect. Immun 2018, 86, No. e00779–17. [PubMed: 29133349]

(22). Gagnon DM; Brophy MB; Bowman SE; Stich TA; Drennan CL; Britt RD; Nolan EM Manganese binding properties of human calprotectin under conditions of high and low calcium: X-ray crystallographic and advanced electron paramagnetic resonance spectroscopic analysis. J. Am. Chem. Soc 2015, 137, 3004–3016. [PubMed: 25597447]

(23). Nakashige TG; Zygiel EM; Drennan CL; Nolan EM Nickel Sequestration by the Host-Defense Protein Human Calprotectin. J. Am. Chem. Soc 2017, 139, 8828–8836. [PubMed: 28573847]

(24). Nakashige TG; Zhang B; Krebs C; Nolan EM Human calprotectin is an iron-sequestering host-defense protein. Nat. Chem. Biol 2015, 11, 765–771. [PubMed: 26302479]

(25). Besold AN; Culbertson EM; Nam L; Hobbs RP; Boyko A; Maxwell CN; Chazin WJ; Marques AR; Culotta VC Antimicrobial action of calprotectin that does not involve metal withholding. Metallomics 2018, 10, 1728–1742. [PubMed: 30206620]

(26). Lee WH; Zygiel EM; Lee CH; Oglesby AG; Nolan EM; Vila AJ Calprotectin-mediated survival of Staphylococcus aureus in coculture with *Pseudomonas aeruginosa* occurs without nutrient metal sequestration. MBio 2025, 16, No. e0384624. [PubMed: 40152583]

(27). Nairn BL; Lonergan ZR; Wang J; Braymer JJ; Zhang Y; Calcutt MW; Lisher JP; Gilston BA; Chazin WJ; de Crecy-Lagard V; Giedroc DP; Skaar EP The Response of *Acinetobacter baumannii* to Zinc Starvation. Cell Host Microbe 2016, 19, 826–36. [PubMed: 27281572]

(28). Hood MI; Mortensen BL; Moore JL; Zhang Y; Kehl-Fie TE; Sugitani N; Chazin WJ; Caprioli RM; Skaar EP; Isberg RR Identification of an *Acinetobacter baumannii* Zinc Acquisition System that Facilitates Resistance to Calprotectin-mediated Zinc Sequestration. PLoS Pathog 2012, 8, No. e1003068. [PubMed: 23236280]

(29). Juttukonda LJ; Chazin WJ; Skaar EP Acinetobacter baumannii Coordinates Urea Metabolism with Metal Import To Resist Host-Mediated Metal Limitation. mBio 2016, 7, No. e01475–16. [PubMed: 27677795]

(30). Moore JL; Becker KW; Nicklay JJ; Boyd KL; Skaar EP; Caprioli RM Imaging mass spectrometry for assessing temporal proteomics: Analysis of calprotectin in Acinetobacter baumannii pulmonary infection. Proteomics 2014, 14, 820–828. [PubMed: 23754577]

(31). Hesse LE; Lonergan ZR; Beavers WN; Skaar EP The *Acinetobacter baumannii* Znu System Overcomes Host-Imposed Nutrient Zinc Limitation. Infect. Immun 2019, 87, No. e00746–19.

(32). Lonergan ZR; Nairn BL; Wang J; Hsu YP; Hesse LE; Beavers WN; Chazin WJ; Trinidad JC; VanNieuwenhze MS; Giedroc DP; Skaar EP An *Acinetobacter baumannii*, Zinc-Regulated Peptidase Maintains Cell Wall Integrity during Immune-Mediated Nutrient Sequestration. Cell Rep 2019, 26, 2009–2018. [PubMed: 30784584]

(33). Wang J; Lonergan ZR; Gonzalez-Gutierrez G; Nairn BL; Maxwell CN; Zhang Y; Andreini C; Karty JA; Chazin WJ; Trinidad JC; Skaar EP; Giedroc DP Multi-metal Restriction by Calprotectin Impacts *De Novo* Flavin Biosynthesis in Acinetobacter baumannii. Cell Chem. Biol 2019, 26, 745–755. [PubMed: 30905682]

(34). Mortensen BL; Rathi S; Chazin WJ; Skaar EP Acinetobacter baumannii response to host-mediated zinc limitation requires the transcriptional regulator zur. J. Bacteriol 2014, 196, 2616–2626. [PubMed: 24816603]

(35). Osterberg MK; Smith AK; Campbell C; Deredge DJ; Stemmler TL; Giedroc DP Coupling of zinc and GTP binding drives G-domain folding in Acinetobacter baumannii ZigA. Biophys. J 2024, 123, 979–991. [PubMed: 38459695]

(36). Jordan MR; Gonzalez-Gutierrez G; Trinidad JC; Giedroc DP Metal retention and replacement in QueD2 protect queuosinet-RNA biosynthesis in metal-starved Acinetobacter baumannii. Proc. Natl. Acad. Sci. U. S. A 2022, 119, No. e2213630119. [PubMed: 36442121]

(37). de Crecy-Lagard V; Jaroch M Functions of Bacterial tRNA Modifications: From Ubiquity to Diversity. Trends Microbiol 2021, 29, 41–53. [PubMed: 32718697]

(38). Wang X; Matuszek Z; Huang Y; Parisien M; Dai Q; Clark W; Schwartz MH; Pan T Queuosine modification protects cognate tRNAs against ribonuclease cleavage. RNA 2018, 24, 1305–1313. [PubMed: 29970597]

(39). Pollo-Oliveira L; Davis NK; Hossain I; Ho P; Yuan Y; Salguero García P; Pereira C; Byrne SR; Leng J; Sze M; Blaby-Haas CE; Sekowska A; Montoya A; Begley T; Danchin A; Aalberts DP; Angerhofer A; Hunt J; Conesa A; Dedon PC; de Crécy-Lagard V The absence of the queuosine tRNA modification leads to pleiotropic phenotypes revealing perturbations of metal and oxidative stress homeostasis in Escherichia coli K12. Metallomics 2022, 14, No. mfac065. [PubMed: 36066904]

(40). Diaz-Rullo J; Gonzalez-Pastor JE tRNA queuosine modification is involved in biofilm formation and virulence in bacteria. Nucleic Acids Res 2023, 51, 9821–9837. [PubMed: 37638766]

(41). Zaborske JM; Bauer DuMont VL; Wallace EWJ; Pan T; Aquadro CF; Drummond DA A nutrient-driven tRNA modification alters translational fidelity and genome-wide protein coding across an animal genus. PLoS Biol 2014, 12, No. e1002015. [PubMed: 25489848]

(42). Osman D; Martini MA; Foster AW; Chen J; Scott AJP; Morton RJ; Steed JW; Lurie-Luke E; Huggins TG; Lawrence AD; Deery E; Warren MJ; Chivers PT; Robinson NJ Bacterial sensors define intracellular free energies for correct enzyme metalation. Nat. Chem. Biol 2019, 15, 241–249. [PubMed: 30692683]

(43). Young TR; Deery E; Foster AW; Martini MA; Osman D; Warren MJ; Robinson NJ Two Distinct Thermodynamic Gradients for Cellular Metalation of Vitamin B(12). JACS Au 2023, 3, 1472–1483. [PubMed: 37234125]

(44). Radin JN; Kelliher JL; Solorzano PKP; Grim KP; Ramezanifard R; Slauch JM; Kehl-Fie TE Metal-independent variants of phosphoglycerate mutase promote resistance to nutritional immunity and retention of glycolysis during infection. PLoS Pathog 2019, 15, No. e1007971. [PubMed: 31344131]

(45). Garcia YM; Barwinska-Sendra A; Tarrant E; Skaar EP; Waldron KJ; Kehl-Fie TE A Superoxide Dismutase Capable of Functioning with Iron or Manganese Promotes the Resistance of *Staphylococcus aureus* to Calprotectin and Nutritional Immunity. PLoS Pathog 2017, 13, No. e1006125. [PubMed: 28103306]

(46). Apuy JL; Chen X; Russell DH; Baldwin TO; Giedroc DP Ratiometric pulsed alkylation/mass spectrometry of the cysteine pairs in individual zinc fingers of MRE-binding transcription factor-1 (MTF-1) as a probe of zinc chelate stability. Biochemistry 2001, 40, 15164–15175. [PubMed: 11735399]

(47). Apuy JL; Busenlehner LS; Russell DH; Giedroc DP Ratiometric Pulsed Alkylation Mass Spectrometry as a Probe of Thiolate Reactivity in Different Metalloderivatives of *Staphylococcus aureus* pI258 CadC. Biochemistry 2004, 43, 3824–3834. [PubMed: 15049689]

(48). Glauninger H; Zhang Y; Higgins KA; Jacobs AD; Martin JE; Fu Y; Coyne Rd HJ; Bruce KE; Maroney MJ; Clemmer DE; Capdevila DA; Giedroc DP Metal-dependent allosteric activation and inhibition on the same molecular scaffold: The copper sensor CopY from *Streptococcus pneumoniae*. Chem. Sci 2018, 9, 105–118. [PubMed: 29399317]

(49). Pace NJ; Weerapana E A competitive chemical-proteomic platform to identify zinc-binding cysteines. ACS Chem. Biol 2014, 9, 258–65. [PubMed: 24111988]

(50). Bak DW; Weerapana E A Chemoproteomic Approach to Monitor Native Iron-Sulfur Cluster Binding. Methods Mol. Biol 2024, 2839, 261–289. [PubMed: 39008260]

(51). Bak DW; Weerapana E Proteomic strategies to interrogate the Fe-S proteome. Biochim Biophys Acta Mol. Cell Res 2024, 1871, No. 119791. [PubMed: 38925478]

(52). Bak DW; Weerapana E Monitoring Fe-S cluster occupancy across the E. coli proteome using chemoproteomics. Nat. Chem. Biol 2023, 19, 356–366. [PubMed: 36635565]

(53). Fisher CE; Bak DW; Miller KE; Washington-Hughes CL; Dickfoss AM; Weerapana E; Py B; Outten FW Escherichia coli monothiol glutaredoxin GrxD replenishes Fe-S clusters to the essential ErpA A-type carrier under low iron stress. J. Biol. Chem 2024, 300, No. 107506. [PubMed: 38944118]

(54). Chan AN; Chen X; Falco JA; Bak DW; Weerapana E; Li B Chemoproteomics Reveals Disruption of Metal Homeostasis and Metalloproteins by the Antibiotic Holomycin. ACS Chem. Biol 2023, 18, 1909–1914. [PubMed: 37561838]

(55). Barrault M; Chabelskaya S; Coronel-Tellez RH; Toffano-Nioche C; Jacquet E; Bouloc P Staphylococcal aconitase expression during iron deficiency is controlled by an sRNA-driven feedforward loop and moonlighting activity. Nucleic Acids Res 2024, 52, 8241–8253. [PubMed: 38869061]

(56). Jordan MR; Dujovne MV; Capdevila DA; Giedroc DP Metal ion homeostasis: Metalloenzyme paralogs in the bacterial adaptaive response to zinc restriction. In Bioinorganic Chemistry and Homogeneous Biomimetic Inorganic Catalysis, Pecoraro VL; Guo Z, Eds.; Elsevier: Oxford, 2022; Vol. 2, pp 30–52.

(57). Ueta M; Wada C; Wada A YkgM and YkgO maintain translation by replacing their paralogs, zinc-binding ribosomal proteins L31 and L36, with identical activities. Genes Cells 2020, 25, 562–581. [PubMed: 32559334]

(58). Pi H; Helmann JD Sequential induction of Fur-regulated genes in response to iron limitation in *Bacillus subtilis*. Proc. Natl. Acad. Sci. U. S. A 2017, 114, 12785–12790. [PubMed: 29133393]

(59). Shin JH; Helmann JD Molecular logic of the Zur-regulated zinc deprivation response in *Bacillus subtilis*. Nat. Commun 2016, 7, 12612. [PubMed: 27561249]

(60). Li Y; Sharma MR; Koripella RK; Yang Y; Kaushal PS; Lin Q; Wade JT; Gray TA; Derbyshire KM; Agrawal RK; Ojha AK Zinc depletion induces ribosome hibernation in mycobacteria. Proc. Natl. Acad. Sci. U. S. A 2018, 115, 8191–8196. [PubMed: 30038002]

(61). Edmonds KA; Jordan MR; Giedroc DP COG0523 proteins: A functionally diverse family of transition metal-regulated G3E P-loop GTP hydrolases from bacteria to man. Metallomics 2021, 13, No. mfab046. [PubMed: 34302342]

(62). Valasatava Y; Rosato A; Banci L; Andreini C Metal-Predator: a web server to predict iron-sulfur cluster binding proteomes. Bioinformatics 2016, 32, 2850–2. [PubMed: 27273670]

(63). Putignano V; Rosato A; Banci L; Andreini C MetalPDB in 2018: A database of metal sites in biological macromolecular structures. Nucleic Acids Res 2018, 46, D459–D464. [PubMed: 29077942]

(64). Pritts JD; Michel SLJ Fe-S clusters masquerading as zinc finger proteins. J. Inorg. Biochem 2022, 230, No. 111756. [PubMed: 35247854]

(65). Lo Sciuto A; D'Angelo F; Spinnato MC; Garcia PS; Genah S; Matteo C; Séchet E; Banin E; Barras F; Imperi F; Storz G A molecular comparison of [Fe-S] cluster-based homeostasis in *Escherichia coli* and *Pseudomonas aeruginosa*. mBio 2024, 15, No. e0120624. [PubMed: 39360836]

(66). Zimbler DL; Park TM; Arivett BA; Penwell WF; Greer SM; Woodruff TM; Tierney DL; Actis LA Stress response and virulence functions of the *Acinetobacter baumannii* NfuA Fe-S scaffold protein. J. Bacteriol 2012, 194, 2884–93. [PubMed: 22467784]

(67). Fleischhacker AS; Stubna A; Hsueh KL; Guo Y; Teter SJ; Rose JC; Brunold TC; Markley JL; Munck E; Kiley PJ Characterization of the [2Fe-2S] cluster of *Escherichia coli* transcription factor IscR. Biochemistry 2012, 51, 4453–4462. [PubMed: 22583201]

(68). Conde-Perez K; Vazquez-Ucha JC; Alvarez-Fraga L; Ageitos L; Rumbo-Feal S; Martinez-Guitian M; Trigo-Tasende N; Rodriguez J; Bou G; Jimenez C; Beceiro A; Poza M In-Depth Analysis of the Role of the Acinetobactin Cluster in the Virulence of Acinetobacter baumannii. Front Microbiol 2021, 12, No. 752070. [PubMed: 34675911]

(69). Bailey DC; Bohac TJ; Shapiro JA; Giblin DE; Wencewicz TA; Gulick AM Crystal Structure of the Siderophore Binding Protein BauB Bound to an Unusual 2:1 Complex Between Acinetobactin and Ferric Iron. Biochemistry 2018, 57, 6653–6661. [PubMed: 30406986]

(70). Valentino H; Korasick DA; Bohac TJ; Shapiro JA; Wencewicz TA; Tanner JJ; Sobrado P Structural and Biochemical Characterization of the Flavin-Dependent Siderophore-Interacting Protein from *Acinetobacter baumannii*. ACS Omega 2021, 6, 18537–18547. [PubMed: 34308084]

(71). Mortensen BL; Rathi S; Chazin WJ; Skaar EP Acinetobacter baumannii response to host-mediated zinc limitation requires the transcriptional regulator Zur. J. Bacteriol 2014, 196, 2616–26. [PubMed: 24816603]

(72). Hood MI; Mortensen BL; Moore JL; Zhang Y; Kehl-Fie TE; Sugitani N; Chazin WJ; Caprioli RM; Skaar EP Identification of an *Acinetobacter baumannii* zinc acquisition system that facilitates resistance to calprotectin-mediated zinc sequestration. PLoS Pathog 2012, 8, No. e1003068. [PubMed: 23236280]

(73). Varghese S; Tang Y; Imlay JA Contrasting sensitivities of Escherichia coli aconitases A and B to oxidation and iron depletion. J. Bacteriol 2003, 185, 221–30. [PubMed: 12486059]

(74). Eijkelkamp BA; Hassan KA; Paulsen IT; Brown MH Investigation of the human pathogen *Acinetobacter baumannii* under iron limiting conditions. BMC Genomics 2011, 12, 126. [PubMed: 21342532]

(75). Ezraty B; Vergnes A; Banzhaf M; Duverger Y; Huguenot A; Brochado AR; Su SY; Espinosa L; Loiseau L; Py B; Typas A; Barras F Fe-S cluster biosynthesis controls uptake of amino-glycosides in a ROS-less death pathway. Science 2013, 340, 1583–7. [PubMed: 23812717]

(76). Weiss A; Murdoch CC; Edmonds KA; Jordan MR; Monteith AJ; Perera YR; Rodríguez Nassif AM; Petoletti AM; Beavers WN; Munneke MJ; Drury SL; Krystofiak ES; Thalluri K; Wu H; Kruse ARS; DiMarchi RD; Caprioli RM; Spraggins JM; Chazin WJ; Giedroc DP; Skaar EP Zn regulated GTPase metalloprotein activator 1 (ZNG1) modulates zinc homeostasis in vertebrates. Cell 2022, 185, 2148–2163. [PubMed: 35584702]

(77). Wisniewski JR Label-Free and Standard-Free Absolute Quantitative Proteomics Using the 'Total Protein' and 'Proteomic Ruler' Approaches. Method Enzymol 2017, 585, 49–60.

(78). Wisniewski JR; Rakus D Multi-enzyme digestion FASP and the 'Total Protein Approach'-based absolute quantification of the *Escherichia coli* proteome. J. Proteomics 2014, 109, 322–31. [PubMed: 25063446]

(79). Gaballa A; Antelmann H; Aguilar C; Khakh SK; Song KB; Smaldone GT; Helmann JD The *Bacillus subtilis* iron-sparing response is mediated by a Fur-regulated small RNA and three small, basic proteins. Proc. Natl. Acad. Sci. U. S. A 2008, 105, 11927–32. [PubMed: 18697947]

(80). Gabriel SE; Helmann JD Contributions of Zur-controlled ribosomal proteins to growth under zinc starvation conditions. J. Bacteriol 2009, 191, 6116–6122. [PubMed: 19648245]

(81). Lin CW; McCabe JW; Russell DH; Barondeau DP Molecular Mechanism of ISC Iron-Sulfur Cluster Biogenesis Revealed by High-Resolution Native Mass Spectrometry. J. Am. Chem. Soc 2020, 142, 6018–6029. [PubMed: 32131593]

(82). Anjem A; Imlay JA Mononuclear iron enzymes are primary targets of hydrogen peroxide stress. J. Biol. Chem 2012, 287, 15544–56. [PubMed: 22411989]

(83). Yang S; Wang Y; Yang Y; Zhang Z; Li F; Tao L; Han L; Guo S; Zhang Y; Jiang Y; Chang J; Yang H Design, Synthesis, and Biological Evaluation of 1,3,4-Thiadiazole Derivatives as Novel Potent Peptide Deformylase Inhibitors for Combating Drug-Resistant Gram-Positive and -Negative Bacteria. J. Med. Chem 2025, 68, 2942–2962. [PubMed: 39772466]

(84). Rohaun SK; Chakraborti PK Oxidation of active site cysteine leads to inactivation of peptide deformylase from *Salmonella enterica*. Biochem. Biophys. Res. Commun 2025, 759, No. 151675. [PubMed: 40147353]

(85). Bradley JM; Carter AM; Bugg Z; Andrews SC; Le Brun NE The Iron-Sulfur Cluster of Bacterioferritin-Associated Ferredoxin (Bfd): a 'Biological Fuse' that Prevents Oxidative Damage to Cells? Angew. Chem., Int. Ed. Engl 2025, 64, No. e202511340. [PubMed: 40531653]

(86). Eren E; Watts NR; Montecinos F; Wingfield PT Encapsulated Ferritin-like Proteins: A Structural Perspective. Biomolecules 2024, 14, 624. [PubMed: 38927029]

(87). Benisch R; Andreas MP; Giessen TW A widespread bacterial protein compartment sequesters and stores elemental sulfur. Sci. Adv 2024, 10, No. eadk9345. [PubMed: 38306423]

(88). Pasquini M; Grosjean N; Hixson KK; Nicora CD; Yee EF; Lipton M; Blaby IK; Haley JD; Blaby-Haas CE Zng1 is a GTP-dependent zinc transferase needed for activation of methionine aminopeptidase. Cell Rep 2022, 39, No. 110834. [PubMed: 35584675]

(89). Critchlow JM; Rocchio JS; McKell MC; Campbell CJ; Barraza JP; Krystofiak ES; Green ER; Akizuki T; Chazin WJ; VanNieuwenhze MS; Stemmler TL; Giedroc DP; Skaar EP The Zinc Metalloprotein MigC Impacts Cell Wall Biogenesis through Interactions with an Essential Mur Ligase in *Acinetobacter baumannii*. PLoS Pathog 2025, 21, No. e1013209. [PubMed: 40523033]

(90). Zhai Y; Zhang X; Chen Z; Yan D; Zhu L; Zhang Z; Wang X; Tian K; Huang Y; Yang X; Sun W; Wang D; Tsai YH; Luo T; Li G Global profiling of functional histidines in live cells using small-molecule photosensitizer and chemical probe relay labelling. Nat. Chem 2024, 16, 1546–1557. [PubMed: 38834725]

(91). Berg JM; Godwin HA Lessons from zinc-binding peptides. Annu. Rev. Biophys. Biomol. Struct 1997, 26, 357–371. [PubMed: 9241423]

(92). Kudva R; Tian P; Pardo-Avila F; Carroni M; Best RB; Bernstein HD; von Heijne G The shape of the bacterial ribosome exit tunnel affects cotranslational protein folding. Elife 2018, 7, No. e36326. [PubMed: 30475203]

(93). Li Y; Majumdar S; Treen R; Sharma MR; Corro J; Gamper HB; Manjari SR; Prusa J; Banavali NK; Stallings CL; Hou YM; Agrawal RK; Ojha AK Starvation sensing by mycobacterial RelA/SpoT homologue through constitutive surveillance of translation. Proc. Natl. Acad. Sci. U. S. A 2023, 120, No. e2302006120. [PubMed: 37216503]

(94). Sinha AK; Winther KS The RelA hydrolase domain acts as a molecular switch for (p)ppGpp synthesis. Commun. Biol 2021, 4, 434. [PubMed: 33790389]

(95). Prossliner T; Skovbo Winther K; Sorensen MA; Gerdes K Ribosome Hibernation. Annu. Rev. Genet 2018, 52, 321–348. [PubMed: 30476446]

(96). Polikanov YS; Blaha GM; Steitz TA How hibernation factors RMF, HPF, and YfiA turn off protein synthesis. Science 2012, 336, 915–8. [PubMed: 22605777]

(97). Guyomar C; D'Urso G; Chat S; Giudice E; Gillet R Structures of tmRNA and SmpB as they transit through the ribosome. Nat. Commun 2021, 12, 4909. [PubMed: 34389707]

(98). Moore SD; Sauer RT The tmRNA system for translational surveillance and ribosome rescue. Annu. Rev. Biochem 2007, 76, 101–24. [PubMed: 17291191]

(99). Schedlbauer A; Iturrioz I; Ochoa-Lizarralde B; Diercks T; López-Alonso JP; Lavin JL; Kaminishi T; Çapuni R; Dhimole N; de Astigarraga E; Gil-Carton D; Fucini P; Connell SR A conserved rRNA switch is central to decoding site maturation on the small ribosomal subunit. Sci. Adv 2021, 7, No. eabf7547. [PubMed: 34088665]

(100). Bennison DJ; Nakamoto JA; Craggs TD; Milón P; Rafferty JB; Corrigan RM; Laub MT The Stringent Response Inhibits 70S Ribosome Formation in Staphylococcus aureus by Impeding GTPase-Ribosome Interactions. mBio 2021, 12, No. e0267921. [PubMed: 34749534]

(101). Linke K; Wolfram T; Bussemer J; Jakob U The roles of the two zinc binding sites in DnaJ. J. Biol. Chem 2003, 278, 44457–44466. [PubMed: 12941935]

(102). Tsirigotaki A; De Geyter J; Sostaric N; Economou A; Karamanou S Protein export through the bacterial Sec pathway. Nat. Rev. Microbiol 2017, 15, 21–36. [PubMed: 27890920]

(103). Callaghan AJ; Redko Y; Murphy LM; Grossmann JG; Yates D; Garman E; Ilag LL; Robinson CV; Symmons MF; McDowall KJ; Luisi BF 'Zn-link': a metal-sharing interface that organizes

the quaternary structure and catalytic site of the endoribonuclease. RNase E. Biochemistry 2005, 44, 4667–4675. [PubMed: 15779893]

(104). Bandyra KJ; Frohlich KS; Vogel J; Rodnina M; Goyal A; Luisi BF Cooperation of regulatory RNA and the RNA degradosome in transcript surveillance. Nucleic Acids Res 2024, 52, 9161–9173. [PubMed: 38842944]

(105). Esakova OA; Grove TL; Yennawar NH; Arcinas AJ; Wang B; Krebs C; Almo SC; Booker SJ Structural basis for tRNA methylthiolation by the radical SAM enzyme MiaB. Nature 2021, 597, 566–570. [PubMed: 34526715]

(106). Mohler K; Ibba M Translational fidelity and mistranslation in the cellular response to stress. Nat. Microbiol 2017, 2, 17117. [PubMed: 28836574]

(107). Eddy SR Profile hidden Markov models. Bioinformatics 1998, 14, 755–763. [PubMed: 9918945]

(108). Freibert SA; Weiler BD; Bill E; Pierik AJ; Muhlenhoff U; Lill R Biochemical Reconstitution and Spectroscopic Analysis of Iron-Sulfur Proteins. Method Enzymol 2018, 599, 197–226.

(109). Marengo M; Puglisi R; Oliaro-Bosso S; Pastore A; Adinolfi S Enzymatic and Chemical In Vitro Reconstitution of Iron-Sulfur Cluster Proteins. Methods Mol. Biol 2021, 2353, 79–95. [PubMed: 34292545]

(110). Cian MB; Giordano NP; Mettlach JA; Minor KE; Dalebroux ZD Separation of the Cell Envelope for Gram-negative Bacteria into Inner and Outer Membrane Fractions with Technical Adjustments for Acinetobacter baumannii. J. Vis. Exp 2020, 158, No. e60517.

(111). Kolaj-Robin O; O'Kane SR; Nitschke W; Leger C; Baymann F; Soulimane T Biochemical and biophysical characterization of succinate: quinone reductase from Thermus thermophilus. Biochim. Biophys. Acta 2011, 1807, 68–79. [PubMed: 20951673]

(112). Shebl B; Menke DE; Pennella M; Poudyal RR; Burke DH; Cornish PV Preparation of ribosomes for smFRET studies: A simplified approach. Arch. Biochem. Biophys 2016, 603, 118–130. [PubMed: 27208427]

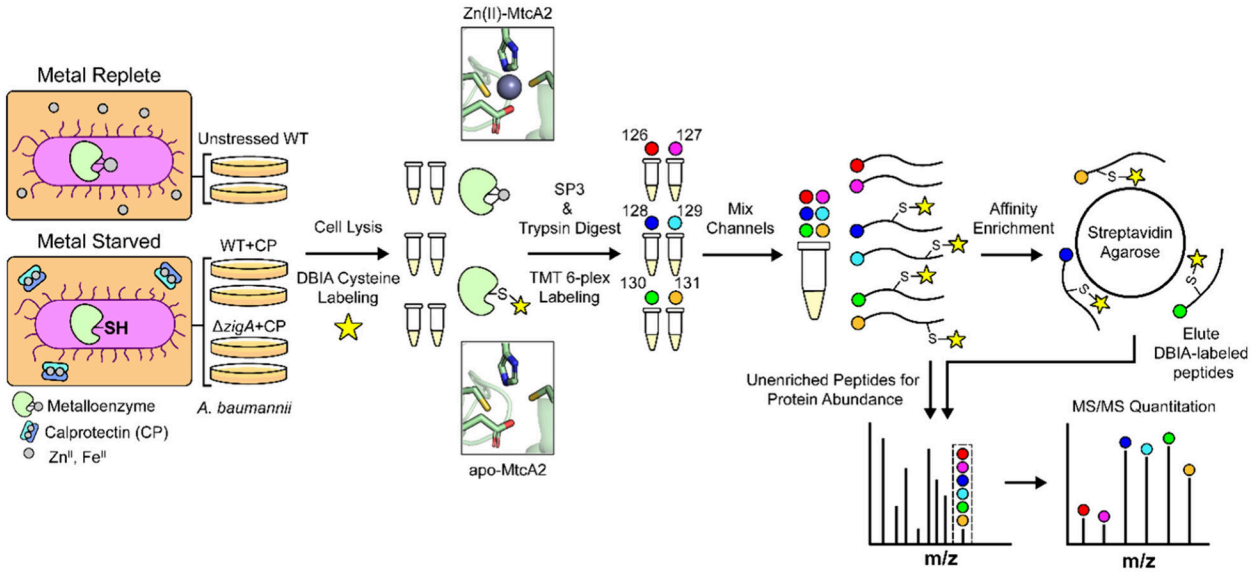

Figure 1.

Schematic representation of the workflow employed in this study. Briefly, biological replicates of each of three bacterial cultures were subjected to cell lysis and thiol labeling, protein isolation and digestion, and derivatization with one of six TMT reagents, as indicated. Samples were mixed at 1:1:1:1:1:1 and this combined sample subjected to either protein abundance quantitation or streptavidin enrichment and cysteine reactivity quantitation by LC-MS/MS. The insets show ribbon representations of Zn(II) bound active site of β-carbonic anhydrase, MtcA2 (*upper*) and apo (metal-free) MtcA2 (*lower*) that might be present in an CP-treated sample (designated undermetalated). See text for additional details.

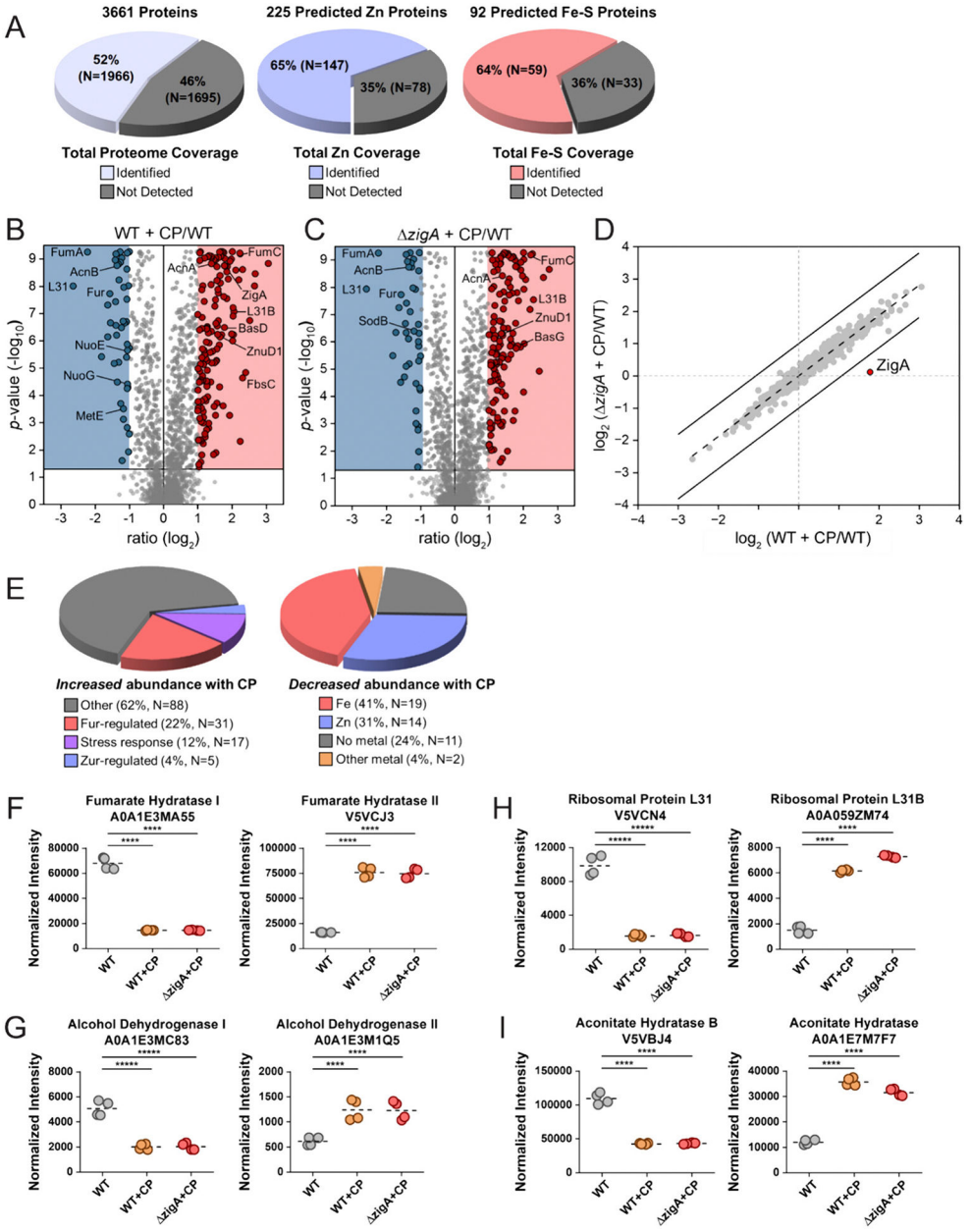

Figure 2.

Change in protein abundance with CP treatment. (A) Pie charts that summarize the statistics of proteome and metalloproteome coverage in these experiments in *A. baumannii* lysates. (B) Volcano plot of WT cells treated with CP vs untreated WT cells. (C) Volcano plot of Δ*zigA* cells treated with CP vs untreated WT cells. (D) log–log plot of CP-mediated changes in the proteomes of WT vs Δ*zigA* cells. *Solid lines*, boundaries of a net fold change of 2 ($\log_2$ fold change = 1) deviating from the trendline (*dashed line*) with the ZigA data point indicated in red. In panel B, 141 proteins increase in cellular abundance ≥ 2-fold (*red* box) while 45 decrease in abundance ≥ 2-fold (*blue* box). (E) Pie charts that summarize the statistical and functional characteristics of *A. baumannii* proteins that increase (*left*; 141 proteins total) or decrease (*right*; 45 proteins) in cell abundance in CP stressed WT cells.

(F)-(I) Normalized intensity of selected protein paralogs that exhibit reciprocal regulation in WT (housekeeping) vs CP-stressed cells. Trivial names for each protein and their Uniprot numbers are indicated. Statistical significance according to an unpaired *t*-test is indicated as follows:*, $p \leq 0.05$; **, $p \leq 0.01$; ***, $p \leq 0.001$; ****, $p \leq 0.0001$.

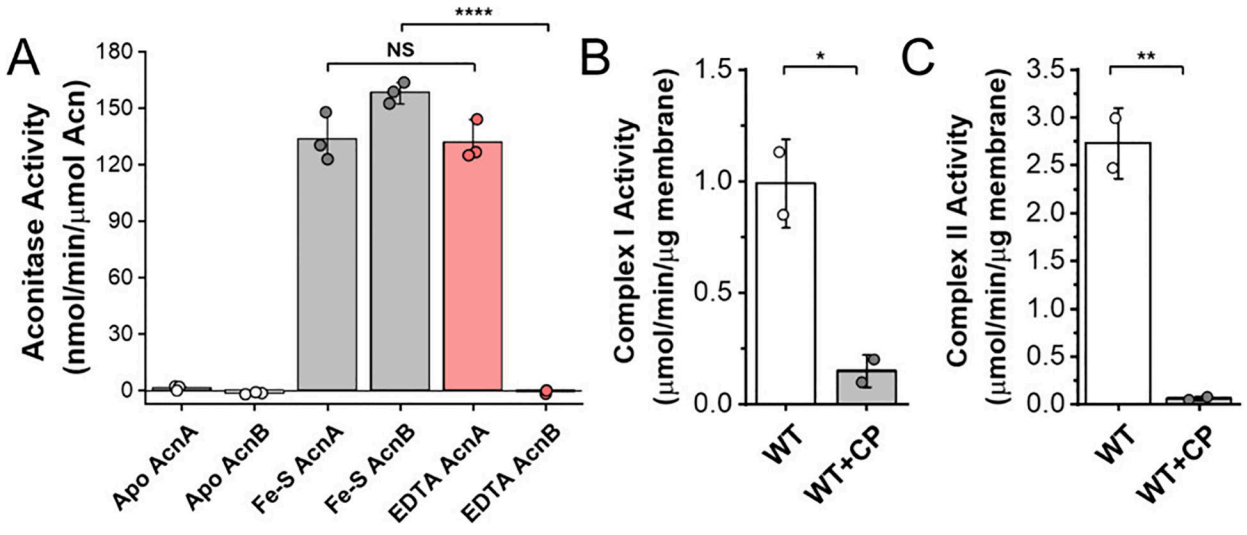

Figure 3.

Measured activities of *A. baumannii* aconitases, complex I, and complex II. (A) Enzyme kinetics of AcnA and AcnB that have been chemically reconstituted with Fe–S clusters and treated with EDTA. (B) Total membrane NADH:ubiquinone dehydrogenase (complex I) activities in biological duplicate as measured by reduction of NADH at 340 nm in untreated (WT) an CP-stressed cells (WT +CP). (C) Total membrane succinate dehydrogenase:ubiquinone oxidoreductase (complex II) activities as measured by reduction of succinate-2,6-dichlorophenolindophenol (DCPIP) at 600 nm in biological duplicate. Significance calculated from an unpaired *t*-test, *, $p \leq 0.05$; **, $p \leq 0.01$; ***, $p \leq 0.001$; ****, $p \leq 0.0001$.

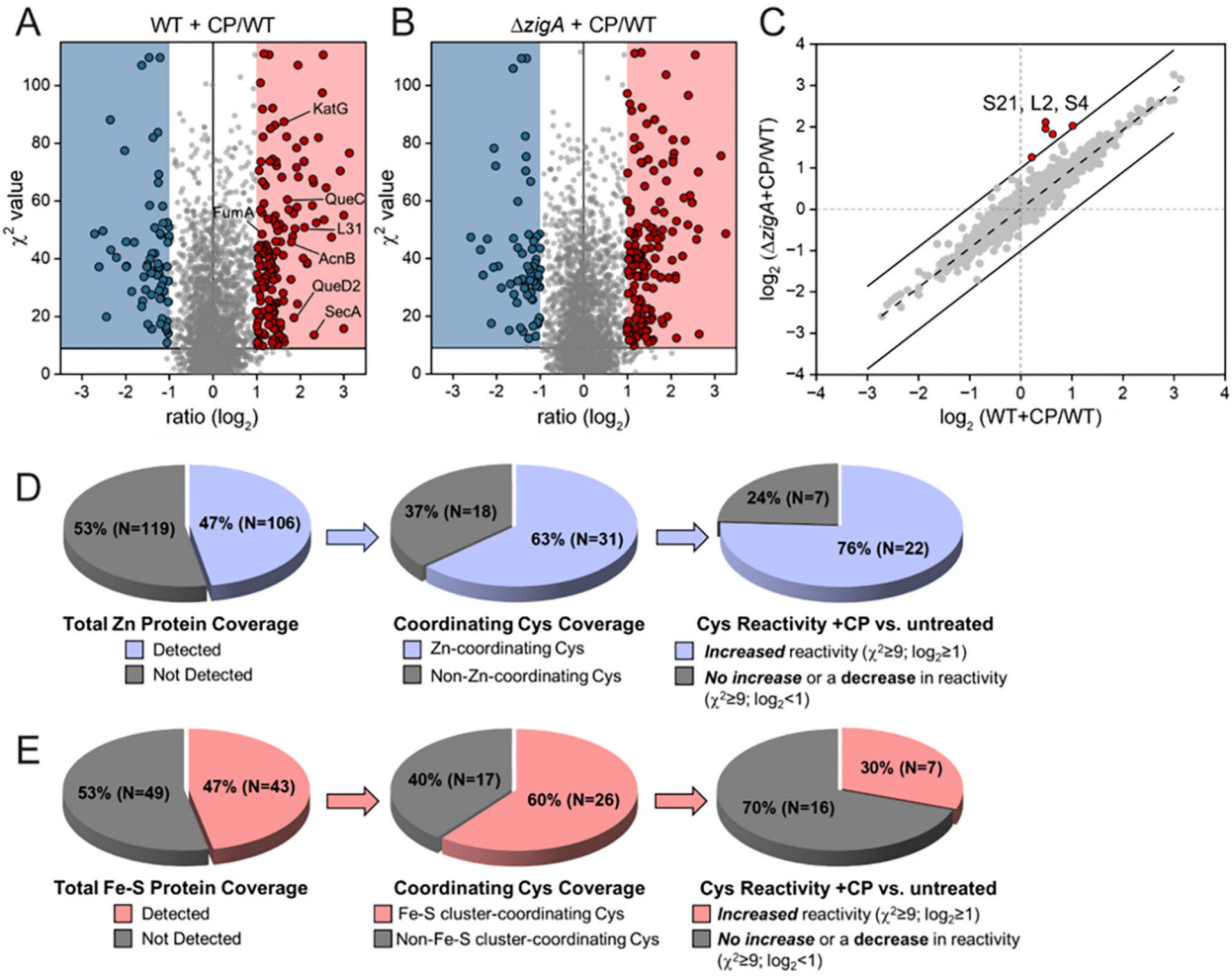

Figure 4.

Change in net Cys reactivity and identification of undermetalated sites in the proteome with CP treatment. (A) wild-type cells treated with CP vs untreated WT cells; (B) Δ*zigA* cells treated with CP vs untreated WT cells. (C) log–log plot of CP-mediated changes in Cys reactivity in the proteomes of WT vs Δ*zigA* cells. *Solid lines*, boundaries of a net fold change of 2 (log_2 fold change = 1) deviating from the trendline (*dashed line*) with the five peptides, corresponding to just three unique Cys, just outside the range indicated; all belong to three ribosomal proteins. (D) Analysis of the Zn metalloproteome. Of the 225 Zn proteins (Document S1), 106 were detected at the peptide level in the Cys reactome (*left* pie chart). 49 of these Zn proteins are predicted to contain a Cys in the first coordination shell, and 31 Cys-containing peptides corresponded to a Zn-ligated Cys (*middle*). Twenty-two out of 29 Cys exhibited a statistically significant change in Cys reactivity using the cut-offs indicated (*right*). An additional four Zn enzymes are identified in this analysis if log_2 cutoff is dropped to 0.64 (1.5-fold increase in Cys reactivity) (Table S1). (E) Analysis of the Fe–S cluster proteome using the same filtering strategy. Of the 92 predicted Fe–S cluster proteins (Document S1), 43 are detected at the peptide level (*left*). Twenty-six of these 43 proteins had a peptide that corresponded to an Fe–S cluster-ligated Cys (*middle*). Seven out of these 23 Cys show a statistically significant change in Cys reactivity using the cut-offs indicated

(*right*). An additional four Fe–S proteins are identified in this analysis if $\log_2$ cutoff is dropped to 0.64 (1.5-fold increase in Cys reactivity) (Table S1).

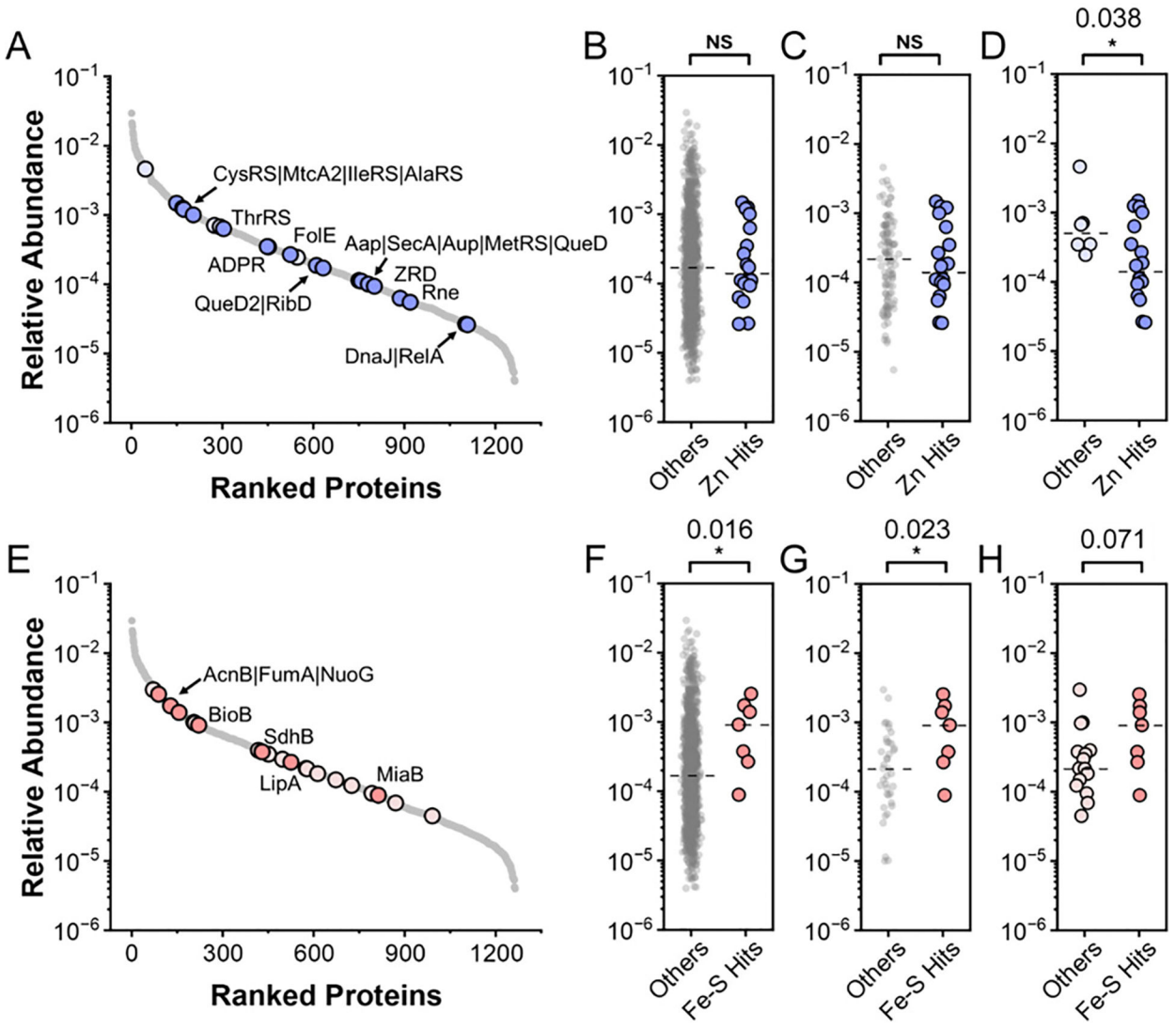

Figure 5.

Analysis of the relative abundance of Zn (A)-(D) and Fe–S cluster (E)-(H) proteins for which Cys reactivity in the first coordination shell could be quantified [panels (A) and (E)] against all proteins in the proteome [panels (B) and (F)], all other Zn or Fe–S metalloproteins detected [panels (C) and (G), respectively], or other metal-sites in Zn- or Fe–S proteins where cysteine reactivity did not reach our significance threshold [panels (D) and (H), respectively]. Filled, dark circles, those metalloproteins that exhibit decreased metal occupancy; light filled circles, those that exhibit no change or decreased Cys reactivity with CP stress. Dotted lines represent the median abundance of each group, with the significance of difference in the medians calculated from a Mann–Whitney *U* analysis and the *p*-values listed above each comparison, *, $p \leq 0.05$; NS, not significant.

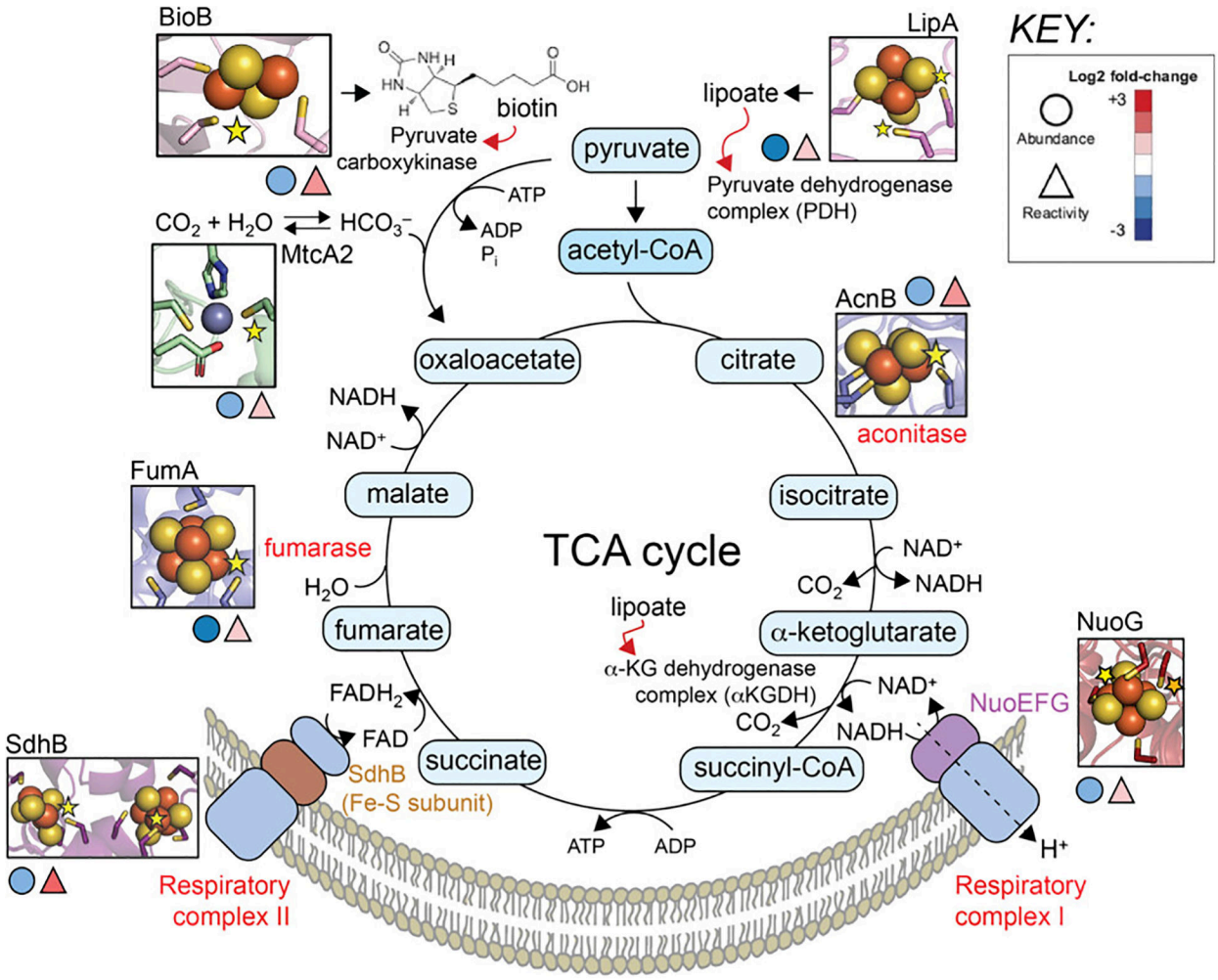

Figure 6.

Schematic illustration of CP-induced undermetalation of enzymes involved in respiration, cofactor biosynthesis and energy transduction. The TCA cycle is coupled to the NADH dehydrogenase respiratory complex I and the succinate dehydrogenase (SDH) complex II. These electrons flow to respiratory complexes III and IV to create the protonmotive force that powers ATP synthesis (not shown). Fe–S and Zn coordination sites are shown, with stars indicating the Cys that become more reactive under conditions of CP stress. Shaded circles and triangles, see key.

Table 1.

List of Selected Proteins Involved in Fe/Zn Homeostasis or the Stress Response That Show Increased Cell Abundance in CP-Stressed Wild-Type (WT+CP) or Δ*zigA (ΔzigA + CP)* vs. WT Untreated Control Cells[a]

Uniprot entry	*KEGG entry*	*description*	gene name	*protein ratio (log2) WT+CP v WT*	*protein ratio (log2) ΔzigA+CP v WT*	*Fur/Zur* [b]	*biological function*
A0A1E3MAV2	A1S_2579	2,3-dihydro-2,3-dihydroxybenzoate dehydrogenase	*fbsD*	**2.66**	**2.20**	Fur	fimsbactin biosynthesis
A0A1E3MAY3	A1S_2570	acetyltransferase	*fbsK*	**2.52**	**2.03**	Fur	fimsbactin biosynthesis
A0A1L5TK40	A1S_2580	2,3-dihydro-2,3-dihydroxybenzoate synthetase	*fbsC*	**2.31**	**2.01**	Fur	fimsbactin biosynthesis
A0A1E3M124	A1S_0771	small-conductance mechanosensitive channel		**2.31**	**2.07**		ion transport
V5VCJ3	A1S_1986	fumarate hydratase class II	*fumC*	**2.24**	**2.22**		TCA cycle
A0A1E3M675	A1S_2390	acinetobactin biosynthesis protein	*basB*	**2.23**	**2.27**	Fur	acinetobactin biosynthesis
A0A059ZM74	A1S_0391	large ribosomal subunit protein bL31B	*rpmE2*	**2.06**	**2.30**	Zur	L31 Zn-sparing paralog
A0A1E3MDH8	A1S_2571	ornithine decarboxylase	*fbsJ*	**2.04**	**1.79**	Fur	fimsbactin biosynthesis
A0A1E3MAZ6	A1S_2572	alcaligin biosynthesis protein	*fbsI*	**2.03**	**1.63**	Fur	fimsbactin biosynthesis
A0A5P1UDU4	A1S_2581	isochorismate synthase	*fbsB*	**2.03**	**1.71**	Fur	fimsbactin biosynthesis
V5VE02	A1S_1950	universal stress protein		**2.02**	**1.92**		stress factor
A0A1E3M655	A1S_2380	isochorismatase	*basF*	**2.01**	**2.01**	Fur	acinetobactin biosynthesis
A0A5P1UDB1	A1S_2574	2,3-dihydroxybenzoate-AMP ligase	*fbsH*	**1.99**	**1.64**	Fur	fimsbactin biosynthesis
A0A1E3M5T3	A1S_1412	glutathione S-transferase		**1.89**	**1.68**		ROS resistance
A0A059ZT15	A1S_2072	universal stress protein		**1.85**	**2.02**		stress factor
A0A1E3M686	A1S_2384	histamine N-monooxygenase	*basC*	**1.79**	**1.76**	Fur	acinetobactin biosynthesis
A0A1E3M8N0	A1S_2381	2,3-dihydroxybenzoate-AMP ligase	*basE*	**1.78**	**1.78**	Fur	acinetobactin biosynthesis
A0A7U4X7Y7	A1S_3411	CobW C-terminal domain-containing protein ZigA	*zigA*	**1.78**	**0.12**	Zur	Zn homeostasis
A0A1E3M6B6	A1S_2383	peptide synthetase	*basD*	**1.78**	**1.70**	Fur	acinetobactin biosynthesis
A0A1E3M653	A1S_2386	ferric anguibactin-binding protein	*bauB*	**1.76**	**1.82**	Fur	acinetobactin import
A0A1E3M3K8	A1S_1654	oxaloacetate decarboxylase	*bfnG*	**1.76**	**1.55**	Fur	baumannoferrin biosynthesis
V5VA41	A1S_2863	AhpC/TSA family protein	*ahpC*	**1.72**	**1.48**		ROS resistance
A0A5P1UFP4	A1S_2566	ligand-gated channel protein	*fbsN*	**1.70**	**1.41**	Fur	fimsbactin import
A0A1E3M3E1	A1S_1652	lucA/IucC family siderophore biosynthesis protein	*bfnE*	**1.67**	**1.44**	Fur	baumannoferrin biosynthesis
A0A1E3M685	A1S_2372	isochorismate synthase	*basJ*	**1.67**	**1.71**	Fur	acinetobactin biosynthesis
V5VE85	A1S_1470	glutathione peroxidase	*bsaA*	**1.66**	**1.62**		ROS resistance
A0A7U4X5T2	A1S_2578	peptide synthetase	*fbsE*	**1.65**	**1.30**	Fur	fimsbactin biosynthesis

Uniprot entry	*KEGG entry*	*description*	gene name	*protein ratio (log2) WT+CP v WT*	*protein ratio (log2) ΔzigA+CP v WT*	*Fur/Zur* [b]	*biological function*
A0A1E3M665	A1S_2391	peptide synthetase	*basA*	**1.64**	**1.55**	Fur	acinetobactin biosynthesis
V5VIG0	A1S_0453	biopolymer transport protein ExbB	*exbB*	**1.63**	**1.66**	Zur	Zn uptake
V5VDG9	A1S_1657	acetyltransferase	*bfnL*	**1.61**	**1.69**	Fur	baumannoferrin biosynthesis
V5VEI3	A1S_1246	universal stress family protein		**1.60**	**1.42**		stress factor
A0A1E3M3G0	A1S_1651	siderophore achromobactin biosynthesis protein AcsC	*bfnD*	**1.59**	**1.46**	Fur	baumannoferrin biosynthesis
A0A7U4X5W9	A1S_2575	peptide synthetase	*fbsG*	**1.58**	**1.21**	Fur	fimsbactin biosynthesis
A0A1E3M7F7	A1S_0558	aconitate hydratase	*acnA*	**1.56**	**1.39**		TCA cycle
A0A1E3M668	A1S_2379	histidine decarboxylase	*basG*	**1.54**	**1.84**	Fur	acinetobactin biosynthesis
A0A059ZIQ0	A1S_1009	copper homeostasis protein	*nlpE*	**1.52**	**1.34**		ROS resistance
A0A1E3M3D7	A1S_1648	ornithine monooxygenase	*bfnB*	**1.49**	**1.27**	Fur	baumannoferrin biosynthesis
A0A1E3M8P2	A1S_2392	NADPH-dependent ferric siderophore reductase	*bauF*	**1.43**	**1.18**	Fur	acinetobactin reductase
A0A1E3MBP6	A1S_2892	TonB-dependent receptor	*znuD1*	**1.40**	**1.38**		Zn uptake
V5VGU2	A1S_0683	ribosome hibernation promoting factor	*raiA*	**1.39**	**1.31**		ribosome hibernation
A0A1E3M7T8	A1S_0452	TonB-dependent receptor	*tonB*	**1.33**	**1.34**	Zur	Zn uptake
A0A5P1UI20	A1S_2582	AraC family transcriptional regulator	*fbsA*	**1.32**	**0.99**	Fur	fimsbactin regulation
A0A1E3MCQ5	A1S_2567	thioesterase	*fbsM*	**1.28**	**1.18**	Fur	fimsbactin biosynthesis
A0A1E3M630	A1S_2378	ABC transporter	*barA*	**1.26**	**1.37**	Fur	acinetobactin export
A0A5P1UK94	A1S_1647	siderophore biosynthesis protein	*bfnA*	**1.19**	**1.17**	Fur	baumannoferrin biosynthesis
V5VGK1	A1S_1186	chaperone protein ClpB	*clpB*	**1.15**	**1.14**		stress factor
A0A059ZN38	A1S_2387	ATP-binding cassette domain-containing protein	*bauE*	**1.15**	**1.22**	Fur	acinetobactin import
A0A1E3M643	A1S_2374	thioesterase	*basH*	**1.14**	**1.36**	Fur	acinetobactin biosynthesis
A0A1L5TMI2	A1S_0146	zinc ABC transporter substrate-binding protein	*znuA*	**1.14**	**1.10**		Zn uptake
V5V9K7	A1S_2834	large-conductance mechanosensitive channel		**1.12**	**1.05**		ion transport
V5VH78	A1S_0454	biopolymer transport ExbD/TolR family protein	*exbD*	**1.11**	**1.12**	Zur	Zn uptake
A0A0E1FM87	A1S_0474	ferric siderophore receptor protein	*bfrD*	**1.11**	**0.99**	Fur	siderophore uptake
V5VI41	A1S_0034	2,3-dihydroxybenzoate-2,3-dehydrogenase	*yciK*	**1.08**	**1.20**	Fur	
A0A1E3M7N8	A1S_0412	catalase-peroxidase	*katG*	**1.06**	**0.97**		stress factor
V5VHL8	A1S_0136	glutathione-S-transferase	*dcmA*	**1.06**	**0.92**		stress factor
A0A1E3M8A1	A1S_0980	outer membrane receptor protein	*pirA*	**1.06**	**1.10**		siderophore uptake
A0A1E3MBF3	A1S_2765	glyoxalase III (protein deglycase)	*hchA*	**1.05**	**1.13**		stress factor

Uniprot entry	*KEGG entry*	*description*	**gene name**	***protein ratio (log2) WT+CP v WT***	***protein ratio (log2) ΔzigA+CP v WT***	***Fur/Zur*** [b]	***biological function***
A0A7U4XBR3	A1S_2076	outer membrane porin		**1.04**	**0.99**		Fe(III)-coprogen receptor
V5VA09	A1S_2692	universal stress protein		**1.01**	**1.08**		stress factor
A0A1E3M2Y5	A1S_1386	catalase	*katE*	**1.00**	**0.83**		ROS resistance
A0A1E3M5 V4	A1S_1411	glutathione-dependent disulfide-bond oxidoreductase		**1.00**	**0.88**		stress factor

[a] See Document S2 for a list of all proteins.

[b] Genes known to be regulated by ferric uptake repressor (Fur) or zinc uptake repressor (Zur).

Table 2.

List of All Proteins That Show Decreased Abundance in CP-Stressed Wild-Type (WT + CP) or ΔzigA (ΔzigA + CP) vs. WT Untreated Control Cells

Uniprot entry	KEGG entry	description	gene name	protein ratio (log2) WT+CP v WT	protein ratio (log2) ΔzigA+CP v WT	metal cofactor
V5VCN4	A1S_2423	large ribosomal subunit protein bL31	*rpmE*	**−2.64**	**−2.58**	Zn
A0A1E3MA55	A1S_0480	fumarate hydratase class I	*fumA*	**−2.22**	**−2.23**	Fe–S cluster
A0A077G9Y2	A1S_0388	aldehyde-activating protein: *S*-hydroxymethylglutathione synthase	*gba*	**−1.81**	**−1.81**	Zn
A0A0Q2HWF1	A1S_0891	hemerythrin		**−1.63**	**−1.72**	Fe
V5VBQ0	A1S_2793	alanine/glycine transport protein	*agcS*	**−1.63**	**−1.63**	
Q9ZAJ4	A1S_0895	ferric uptake regulation protein	*fur*	**−1.57**	**−1.57**	Fe
V5V915	A1S_3104	ATP-dependent RNA helicase	*deaD*	**−1.55**	**−1.42**	
A0A5P1UI52	A1S_3029	tRNA-2-methylthio-N(6)-dimethylallyladenosine synthase	*miaB*	**−1.44**	**−1.42**	Fe–S cluster
V5VGV9	A1S_0378	electron transfer flavoprotein-ubiquinone oxidoreductase	*etfD*	**−1.41**	**−1.38**	Fe–S cluster
A0A1L5TSN5	A1S_1674	DUF2797 domain-containing protein		**−1.40**	**−1.41**	
A0A1L5TJN1	A1S_2433	5′-nucleotidase SurE	*surE*	**−1.39**	**−1.44**	other metal
A0A5P1UKT1	A1S_0020	isoleucine–tRNA ligase	*ileS*	**−1.39**	**−1.42**	Zn
V5VAD3	A1S_2714	succinate dehydrogenase iron–sulfur subunit	*sdhB*	**−1.37**	**1.35**	Fe–S cluster
V5VBJ4	A1S_2126–2128	aconitate hydratase B	*acnB*	**−1.36**	**−1.34**	Fe–S cluster
V5VAK6	A1S_2712	succinate dehydrogenase hydrophobic membrane anchor subunit	*sdhD*	**−1.35**	**−1.47**	Fe
V5VFR9	A1S_0984	carbonic anhydrase (*β*-class)	*mtcA2*	**−1.32**	**−1.26**	Zn
A0A1E3MC83	A1S_3436	alcohol dehydrogenase		**−1.31**	**−1.33**	Zn
A0A059ZUZ0	A1S_1511	biotin synthase	*bioB*	**−1.30**	**−1.22**	Fe–S cluster
V5VBJ6	A1S_2329	lipoyl synthase	*lipA*	**−1.27**	**−1.30**	Fe–S cluster
A0A059ZJ19	A1S_0756	NADH-quinone oxidoreductase subunit F	*nuoF*	**−1.26**	**−1.27**	Fe–S cluster
V5V8Q5	A1S_3405	histidine ammonia-lyase	*hutH*	**−1.25**	**−1.58**	
V5VID1	A1S_0486	gluconokinase	*gntK*	**−1.23**	**−1.06**	
V5VDU6	A1S_1631	iron–sulfur cluster assembly scaffold protein IscU	*iscU*	**−1.22**	**−1.20**	Fe–S cluster
A0A7U4X6J8	A1S_3859	DUF4393 domain-containing protein		**−1.21**	**−1.08**	
V5VBX8	A1S_2713	succinate dehydrogenase flavoprotein subunit	*sdhA2*	**−1.18**	**−1.30**	
A0A5P1UIL0	A1S_0737	5-methyltetrahydropteroyltriglutamate–homocysteine methyltransferase	*metE*	**−1.17**	**−1.13**	Zn
A0A0E1FDM9	A1S_0922	homocysteine S-methyltransferase	*mmuM*	**−1.17**	**−1.07**	Zn
V5VDL9	A1S_1633	cysteine desulfurase IscS	*iscS*	**−1.16**	**−1.15**	Fe–S cluster

ACS Chem Biol. Author manuscript; available in PMC 2026 January 13.

Uniprot entry	KEGG entry	description	gene name	protein ratio (log2) WT+CP v WT	protein ratio (log2) ΔzigA+CP v WT	metal cofactor
V5VJC1	A1S_0071	aminotransferase	*tyrB*	**−1.14**	**−1.04**	
A0A059ZMZ4	A1S_1235	cysteine-tRNA ligase	*cysS*	**−1.08**	**−1.06**	Zn
A0A0D7SED5	A1S_1698	lipoyl synthase	*lipA*	**−1.08**	**−1.05**	Fe–S cluster
V5VBX3	A1S_2708	tRNA uridine(34) hydroxylase	*yibN*	**−1.07**	**−1.05**	
V5VCQ8	A1S_1928	DUF2057 domain-containing protein		**−1.07**	**−0.97**	
V5VAB5	A1S_2775	adenosine 5′-phosphosulfate reductase	*cysH*	**−1.06**	**−1.13**	Fe–S cluster
A0A1E3M509	A1S_0713	quinolinate synthase	*nadA*	**−1.06**	**−1.13**	Fe–S cluster
A0A0Q1DQ33	A1S_2426	lactoylglutathione lyase	*gloA*	**−1.06**	**−1.05**	Zn
V5VHN5	A1S_0286	large ribosomal subunit protein bL12	*rplL*	**−1.06**	**−0.87**	
V5VHU8	A1S_0755	NADH-quinone oxidoreductase subunit E	*nuoE*	**−1.05**	**−1.00**	Fe–S cluster
A0A098SGG9	A1S_0757	NADH-quinone oxidoreductase subunit G	*nuoG*	**−1.05**	**−1.02**	Fe–S cluster
A0A5P1UHV7	A1S_0705	ribulose-phosphate 3-epimerase	*rpe*	**−1.04**	**−1.01**	Zn
V5V9P7	A1S_3060	large ribosomal subunit protein bL36	*rpmJ*	**−1.02**	**−0.96**	Zn
V5VHZ3	A1S_0736	DUF1852 domain-containing protein		**−1.02**	**−1.05**	
A0A1E3MAB1	A1S_3455	dihydroxy-acid dehydratase	*ilvD*	**−1.00**	**−1.03**	Fe–S cluster
V5VAU8	A1S_2343	superoxide dismutase	*sodB*	**−1.00**	**−1.19**	other metal
V5VG06	A1S_0953	cupin		**−1.00**	**−0.45**	other metal

Table 3.

List of Zn or Fe–S Cluster Harboring Proteins and Their Cys-Coordinating Residues That Show Increased Reactivity in CP-Stressed Wild-Type (WT + CP) or CP-Stressed Δ*zigA* (Δ*zigA* + CP) vs. WT Untreated Control Cells[a]

Uniprot entry	KEGG entry	description	gene name	modification position (Cys)	net Cys ratio (log2) WT+CP v WT	net Cys ratio (log2) ΔzigA+CP v WT	metal cofactor
V5V8K0	A1S_3443	chaperone protein DnaJ	*dnaJ*	164	**3.00**	**2.65**	Zn
A0A5P1UGY3	A1S_0221	riboflavin biosynthesis protein RibD	*ribD*	88	**2.72**	**2.59**	Zn
A0A059ZTZ6	A1S_0592	threonine--tRNA ligase	*thrRS*	333|335	**2.55**	**2.63**	Zn
A0A0H4UCN7	A1S_3619	zinc ribbon domain-containing protein		6	**2.16**	**2.11**	Zn
A0A1E3MBL8	A1S_2821	alkylphosphonate utilization protein		6	**2.10**	**2.04**	Zn
A0A1E3MBS1	A1S_2862	protein translocase subunit SecA	*secA*	903	**2.32**	**2.13**	Zn
A0A086HW53	A1S_0531	small ribosomal subunit biogenesis GTPase RsgA	*engC*	319	**2.07**	**2.03**	Zn
A0A1V3DEG5	A1S_2542	7-cyano-7-deazaguanine synthase	*queC*	190	**1.93**	**1.84**	Zn
V5VCN4	A1S_2423	large ribosomal subunit protein bL31	*rpmE*	38|41	**1.88**	**1.81**	Zn
A0A081GYS3	A1S_1566	6-carboxy-5,6,7,8-tetrahydropterin synthase	*queD2*	18	**1.86**	**1.54**	Zn
V5VBJ4	A1S_2126–2128	aconitate hydratase B	*acnB*	718	**1.80**	**1.72**	Fe–S cluster
V5VAD3	A1S_2714	succinate dehydrogenase iron–sulfur subunit	*sdhB*	210|214	**1.79**	**1.77**	Fe–S cluster
A0A059ZTE3	A1S_1176	alanine--tRNA ligase	*alaRS*	670	**1.71**	**1.75**	Zn
A0A0H4UDV2	A1S_2114	DNA mismatch repair protein MutL	*mutL*	596	**1.49**	**1.42**	Zn
A0A059ZMZ4	A1S_1235	cysteine--tRNA ligase	*cysRS*	30	**1.47**	**1.63**	Zn
A0A059ZUZ0	A1S_1511	biotin synthase	*bioB*	128	**1.46**	**1.41**	Fe–S cluster
A0A077G9Y2	A1S_0388	*S*-hydroxymethylglutathione synthase	*gfa*	33	**1.39**	**1.59**	Zn
V5VFR9	A1S_0984	carbonic anhydrase (*β*-class)	*mtcA2*	50	**1.37**	**1.19**	Zn
A0A1E3M178	A1S_0778	methionine--tRNA ligase	*metRS*	142	**1.37**	**1.25**	Zn
V5VGB8	A1S_0696	ADP-ribose pyrophosphatase		26|29	**1.29**	**1.32**	Zn
V5V9P7	A1S_3060	large ribosomal subunit protein bL36	*rpmJ*	11	**1.26**	**1.35**	Zn
A0A1E3M9N2	A1S_0403	ribonuclease E	*rne*	401	**1.19**	**1.12**	Zn
A0A098SGG9	A1S_0757	NADH-quinone oxidoreductase	*nuoG*	235	**1.13**	**1.26**	Fe–S cluster
A0A1E3MA55	A1S_0480	fumarate hydratase class I	*fumA*	264|277	**1.13**	**1.07**	Fe–S cluster
V5VBH1	A1S_2366	GTP cyclohydrolase 1	*folE*	144	**1.09**	**1.24**	Zn
V5VBJ6	A1S_2329	lipoyl synthase	*lipA*	95|98	**1.07**	**0.98**	Fe–S cluster
V5VI79	A1S_0579	GTP pyrophosphokinase	*relA*	662	**1.05**	**1.08**	Zn

Uniprot entry	KEGG entry	description	gene name	modification position (Cys)	net Cys ratio (log2) WT+CP v WT	net Cys ratio (log2) ΔzigA+CP v WT	metal cofactor
A0A5P1UI52	A1S_3029	tRNA-2-methylthio-N(6)-dimethylallyladenosine synthase	*miaB*	40	**1.05**	**1.29**	Fe–S cluster
A0A5P1UKT1	A1S_0020	isoleucine--tRNA ligase	*ileRS*	418	**1.03**	**1.02**	Zn

[a]The Cys shown corresponds to the highest net change in Cys reactivity in the chelate. If two Cys are shown, these correspond to Cys within the same tryptic peptide. The net reactivity changes of other Cys residues associated with these chelates are given in Table S2.